



# Thermodynamic Analysis of a Conceptual Fixed-Bed Solar Thermochemical Cavity Receiver–Reactor Array for Water Splitting Via Ceria Redox Cycling

Song Yang<sup>1,2</sup>, Lifeng Li<sup>2</sup>, Bo Wang<sup>2</sup>, Sha Li<sup>2</sup>, Jun Wang<sup>1\*</sup>, Peter Lund<sup>1,3</sup> and Wojciech Lipiński<sup>2\*</sup>

<sup>1</sup>Key Laboratory of Solar Energy Science and Technology in Jiangsu Province, School of Energy and Environment, Southeast University, Nanjing, China, <sup>2</sup>College of Engineering and Computer Science, The Australian National University, Canberra, ACT, Australia, <sup>3</sup>School of Science, The Aalto University, Espoo, Finland

## OPEN ACCESS

### Edited by:

Alfonso Chinnici,  
University of Adelaide, Australia

### Reviewed by:

Limei Shen,  
Huazhong University of Science and  
Technology, China  
Mahyar Silakhori,  
University of Adelaide, Australia

### \*Correspondence:

Wojciech Lipiński  
wojciech.lipinski@anu.edu.au  
Jun Wang  
wj-jw@seu.edu.cn

### Specialty section:

This article was submitted to  
Process and Energy Systems  
Engineering,  
a section of the journal  
Frontiers in Energy Research

**Received:** 26 May 2020

**Accepted:** 12 May 2021

**Published:** 24 June 2021

### Citation:

Yang S, Li L, Wang B, Li S, Wang J,  
Lund P and Lipiński W (2021)  
Thermodynamic Analysis of a  
Conceptual Fixed-Bed Solar  
Thermochemical Cavity  
Receiver–Reactor Array for Water  
Splitting Via Ceria Redox Cycling.  
*Front. Energy Res.* 9:565761.  
doi: 10.3389/fenrg.2021.565761

We propose a novel solar thermochemical receiver–reactor array concept for hydrogen production via ceria redox cycling. The receiver–reactor array can improve the solar-to-fuel efficiency by realizing the heat recuperation, reduction, and oxidation processes synchronously. A linear matrix model and a lumped parameter model are developed to predict thermal performance of the new solar thermochemical system. The system thermal performance is characterized by heat recovery effectiveness of solid-phase and solar-to-fuel efficiency. Investigated parameters include reduction temperature, oxygen partial pressure, number of receiver–reactors, concentration ratio, and gas-phase heat recovery effectiveness. For baseline conditions, the solid-phase heat recovery effectiveness and the solar-to-fuel efficiency are found to be 81% and 27%, respectively. For perfect gas-phase heat recovery and a solar concentration ratio of 5,000, the solar-to-fuel efficiency exceeds 40%.

**Keywords:** solar thermochemistry, water splitting, non-stoichiometry, cerium oxide, heat recovery

## INTRODUCTION

Solar fuels offer great promise to a sustainable future and can be produced via several pathways such as photo-, electro-, and thermochemical processes, as well as their various combinations (Steinfeld, 2005). Compared to the other processes, the solar thermochemical approach utilizes the entire solar spectrum, allowing for higher theoretical solar-to-fuel efficiency (Steinfeld, 2005; Siegel et al., 2013; Muhich et al., 2016; Bader and Lipiński, 2017). In particular, the two-step non-stoichiometric based redox cycles have been an attractive research area over the past decade (Chueh and Haile, 2010; Furler et al., 2012a; Marxer et al., 2017; Steinfeld, 2019; Qian et al., 2021). Synthesis gas (syngas, a mixture of H<sub>2</sub> and CO) can be produced in two steps. In the first, endothermic step, a metal oxide is non-stoichiometrically reduced, driven by concentrated solar irradiation. In the second, exothermic

**Abbreviations:** 0D, zero dimensional; CPC, compound parabolic concentrator; CRR, cavity receiver–reactor; DNI, direct normal irradiance; HTF, heat transfer fluid; HXer, heat-exchanger; LMM, linear matrix model; LPM, lumped parameter method; RPC, reticulated porous ceria; TR, tower reflector.

step, the reduced metal oxide is oxidized with the H<sub>2</sub>O and/or CO<sub>2</sub> and H<sub>2</sub> and/or CO are produced, respectively.

A key figure of merit to assess the commercial viability of the solar thermochemical pathway for fuel production is the solar-to-fuel efficiency (defined in Eq. 26). A threshold efficiency value of 20% has been suggested to compete with low-risk approaches such as electrolysis (Siegel et al., 2013). Although solar thermochemical water splitting has a high theoretical solar-to-fuel conversion efficiency of 75% (Steinfeld, 2005), to date the experimental record of this technology is only 5.25% for splitting of CO<sub>2</sub> into CO and O<sub>2</sub> (Marxer et al., 2017).<sup>1</sup> Improvement of the solar-to-fuel efficiency critically relies on the development of both superior redox materials and novel reactor designs (Lapp et al., 2012; Miller et al., 2014; Hathaway et al., 2016; Muhich et al., 2018; Li et al., 2021). A wide variety of non-stoichiometric redox materials have been investigated, including pure and doped ceria, as well as perovskites (Chueh et al., 2010; Hao et al., 2014; Qian et al., 2021). Among these candidates, undoped ceria offers a great promise for efficient fuel production due to its fast kinetics, robust cyclability, and high selectivity, and is thus selected as the model material in this study (Abanades et al., 2010; Chueh et al., 2010; Furler et al., 2012b; Marxer et al., 2017).

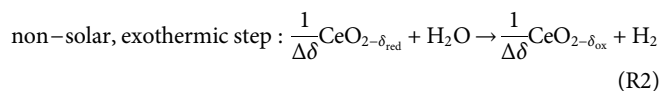
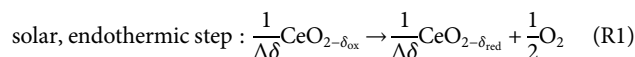
Many reactor designs were proposed and tested with the ultimate goal of improving the solar-to-fuel efficiency (Chueh et al., 2010; Diver et al., 2010; Lapp et al., 2013; Dähler et al., 2018; Wang et al., 2020; Wang et al., 2021). They can be categorized into designs with solid and/or gas heat recuperation (Ermanoski et al., 2013; Lapp and Lipiński, 2014; Hathaway et al., 2016) and designs without heat recuperation (Welte et al., 2016; Marxer et al., 2017). The majority of the reactor systems demonstrated so far are based on the fixed-bed type due to the design simplicity and convenient operation (Chueh et al., 2010; Furler et al., 2012b; Hathaway et al., 2016; Marxer et al., 2017; Haeussler et al., 2020; Sun-to-liquid, 2020). However, a key challenge associated with designing an efficient fixed-bed reactor system is to recover the solid sensible heat under temperature-swing cycling due to the immobility of the redox material. This is particularly relevant when using undoped ceria because its efficiency is critically limited by the energy penalty to heat the solid phase (Hathaway et al., 2016; Muhich et al., 2018; Li et al., 2021). A multi-chamber fixed-bed reactor concept was developed by Yuan et al. that allows for solid heat recuperation by using liquid metal as the heat transfer fluid. This concept promises a thermal-to-chemical efficiency of 20% and a heat recovery effectiveness of 80%, but at the expense of complicated design and operation (Yuan et al., 2015). A more generic design concept incorporating counterflow solid heat exchange was proposed by Falter et al., though the design poses technical challenges to practical operation of moving the high-temperature redox materials (Falter et al., 2015). Besides, a new receiver–reactor system with integrated thermozone heat recovery was proposed but lacks theoretical or experimental

investigations (Steinfeld et al., 2019). To our best knowledge, realizing efficient solid-phase heat recovery in the fixed-bed reactor system with a simple design and operating strategy is absent in the literature.

In our previous work, we proposed a modified solar beam-down system for realizing solid-phase heat recovery for the fixed-bed reactor configuration, where the analysis of the optical system was presented in detail (Li et al., 2020b). In the present work, we introduce the design of the array of receiver–reactors, coupled to the beam-down system, together with the operating strategy for realizing solid-phase heat recovery. The main merits of this work are: (i) the heat recovery is realized without the need of moving redox materials; (ii) the heat of the solid phase is recovered by the direct gas–solid heat exchange in series; and (iii) hydrogen is produced continuously. The model receiver–reactor system comprising recuperation, reduction, and oxidation zones is introduced in “**Problem Statement**” section. Model assumptions, as well as mathematical models, are described in sections “**Methodology and Assumptions**” and “**Mathematical Model**”. Section “**Results and Discussion**” presents the assessment of the heat recovery effectiveness from the solid phase and the sensitivity analysis of the total solar-to-fuel efficiency depending on key parameters, including reduction temperature, relative oxygen partial pressure, receiver–reactor numbers, concentration ratio, and gas-phase heat recovery effectiveness.

## PROBLEM STATEMENT

Thermochemical water splitting (WS) process based on two-step ceria redox cycles is considered in this study:



where  $\Delta\delta = \delta_{\text{red}} - \delta_{\text{ox}}$  is the change in non-stoichiometry.

**Figure 1** depicts the schematic of the proposed beam-down thermochemical system featuring a heliostat field, a tower, a rotating hyperboloidal tower reflector (TR), and a stationary cavity receiver–reactor (CRR) array coupled with compound parabolic concentrators (CPCs) (Li et al., 2020b). The rotating TR directs the concentrated solar irradiation alternately to each CRR through the aperture of the CPCs. Since the focus of this paper is on the reactor system, the radiative input from the optical system is modeled here in a simplified manner assuming step-wise irradiation.

**Figure 2** shows an example of an 8-CRR array that is arranged in a circular layout and fixed on a pedestal (not shown). The system is divided into three zones: reduction (red), oxidation (blue), recuperation (including pre-heating and pre-cooling subzones, yellow) zones. The same amount of the monolithic reticulated porous ceria (RPC) is contained in each CRR.<sup>2</sup> The reduction reaction is realized in the CRR

<sup>1</sup>A higher solar-to-fuel efficiency of 7.5% was reported by (Haeussler et al., 2020) where the realistic parasitic energy consumption is not accounted for.

<sup>2</sup>RPC and Al<sub>2</sub>O<sub>3</sub>-made containers have been successfully demonstrated in a series of solar thermochemical water/CO<sub>2</sub> splitting systems. Assessment of potential materials issues is beyond the scope of this study.

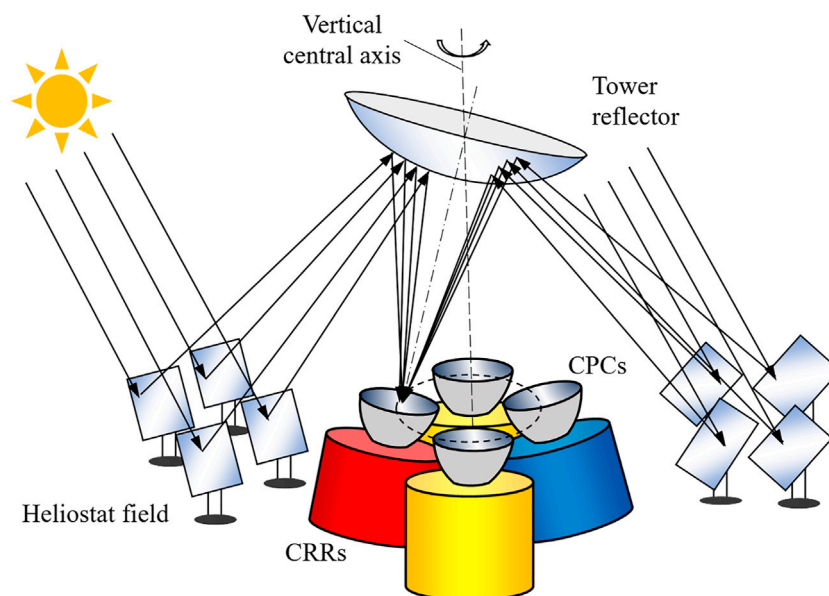


**FIGURE 1** | Schematic of the proposed solar thermochemical system consisting of a heliostat field, a beam-down reflector, and a cavity receiver–reactor array. This figure is adapted from (Li et al., 2020b).

irradiated by the concentrated sunlight (red). The oxidation reaction is realized in the CRR on the opposite side (blue). All other CRRs (yellow) are separated by the central axis into two groups, and heat is exchanged between the two groups. To reduce the emission loss, the aperture of the receiver–reactor is opened only when being irradiated by the concentrated sunlight, and is kept closed otherwise. The CRRs are connected to the neighboring ones and to the gas-phase heat exchangers via pipes. Therefore, the inert gas and water flow through each receiver–reactor to sweep the RPC alternately.

As the rotating TR directs the concentrated sunlight to the stationary CRR array in a clockwise manner, the CRR array can be viewed as “rotating” counter-clockwise relative to the position of concentrated solar irradiation. The operating procedure for one cycle duration  $\tau$  is shown in **Figure 3**. States 1 and 2 represent the beginning of the  $n$ th cycle, and the time instant after “rotating” the CRR array counter-clockwise in one phase, respectively. The transition from State 1 to 2 is assumed instantaneous and thus both states are treated to occur at the same time instant  $(n-1)\tau$ . States 3 and 4 represent the initial and final states of the thermochemical process of the  $n$ th cycle, respectively. For ensuring the synchronization of reduction, oxidation, and recuperation processes, the duration of States 3 and 4,  $\tau$ , is determined by the duration of the reduction step, and the other two processes are proceeding simultaneously for the same duration  $\tau$  by adjusting the flow rates of water and sweep gas. After a complete cycle, the system returns to State 1.

## Reduction Zone

As shown in **Figure 3**, we assume that the CRR array rotates counter-clockwise by one phase during a change from State 1 to

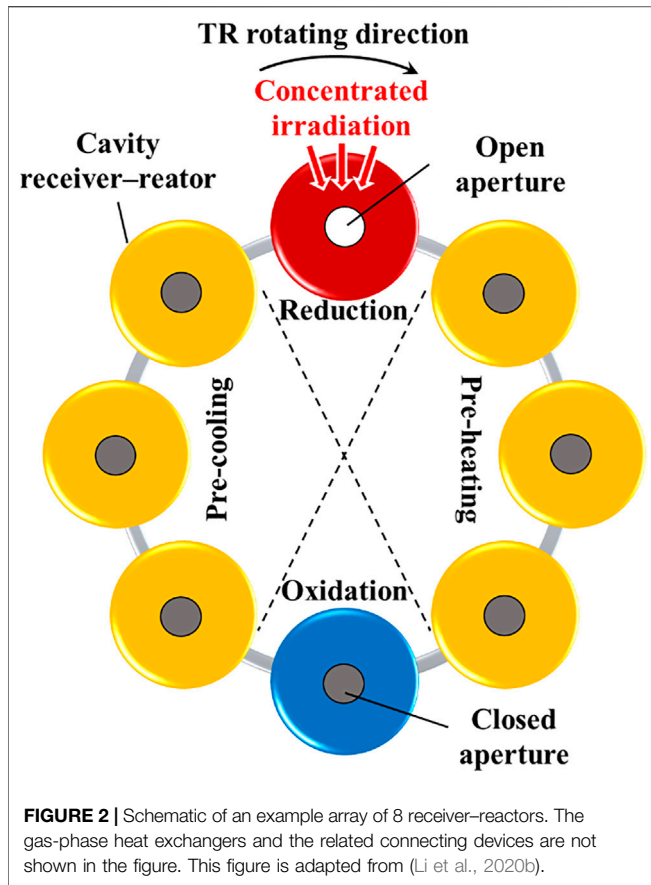
State 2.<sup>3</sup> Therefore, the CRR in  $\#(N+1)$  position of the recuperation zone moves into the reduction zone, where it will be irradiated by concentrated solar irradiation. Then, pure  $N_2$  is used to sweep RPC of the CRR in the reduction zone and to keep rejecting released  $O_2$  from porous media surfaces during the change from State 3 to State 4. The thermal energy of the product gas, the mixture of  $N_2$  and  $O_2$ , is recovered to heat the inlet flow of  $N_2$  by using an indirect gas-phase heat exchanger ( $HXer_1$ ). A reduction period finishes when the thermodynamic state ( $T_{red}, p_{O_2,red}$ ) is reached. The settings of  $T_{red}$  and  $p_{O_2,red}$  values are discussed in “**Results and Discussion**” section. Because the solar-to-fuel efficiency is affected by the feeding strategy of  $N_2$ , the following simplified approach of controlling the  $N_2$  flow rate per kilogram of ceria  $r_{N_2}$  is used: (i) set an initial value of  $r_{N_2} = 10^{-3} \text{ kg s}^{-1} \text{ kg}^{-1}$ ; (ii) continuously adjust  $r_{N_2}$  to approximate the default final relative oxygen partial pressure. The  $N_2$  feeding strategy is illustrated in detail in “**Mathematical Model**” section.

## Recuperation Zone

The recuperation zone is composed of one gas-phase heat exchanger ( $HXer_3$ ) and  $2N$  CRRs (yellow) with one half undergoing pre-cooling (from #1 to # $N$ ) and another half undergoing pre-heating (from  $\#(N+1)$  to # $2N$ ) as labeled in **Figure 3**.

$N_2$  is used as the sweep gas for oxygen scavenger and heat transfer fluid (HTF). A pure cold  $N_2$  flow first goes into an indirect gas-phase heat exchanger ( $HXer_3$ ) where it is heated by the heat of product gases, namely, a mixture of  $N_2$  and  $O_2$ . The

<sup>3</sup>One phase difference represents the angle difference between two adjacent cavities:  $\Delta\theta = \frac{2\pi}{2N+2}$ .



mixture gas then flows continuously through the pre-cooling part from #1 to #N to cool the RPC material in each CRR. The sweep gas reaches the peak temperature when leaving #N, and then goes through the pre-heating part from #(N+1) to #2N to heat the RPC material. The state of ceria in each CRR is updated from  $(T_i^{(n-1)\tau}, \delta_i^{(n-1)\tau})$  to  $(T_i^{n\tau}, \delta_i^{n\tau})$  during the change from States 3 to 4, where the subscript  $i$  represents the  $i$ th CRR position (#i) in the recuperation zone. The superscript  $n\tau$  indicates a time instant.<sup>4</sup> Note that reduction may occur along with heat recovery processes in the recuperation zone. A detailed systematic study is presented in section “Mathematical Model”.

### Oxidation Zone

According to **Figure 3**, the CRR in #1 position of the recuperation zone containing the reduced ceria ( $\text{CeO}_{2-\delta_{\text{red}}}$ ) moves into the oxidation zone during the change from State 1 to State 2, where it will undergo the oxidation reaction. Then,  $\text{CeO}_{2-\delta_{\text{red}}}$  is oxidized at constant oxidation temperature  $T_{\text{ox}}$  by water steam during the change from State 3 to State 4, while  $\text{H}_2$  is generated. Note that ceria needs to be cooled before undergoing the oxidation process. Because the oxidation step is exothermic, the redundant heat generated during oxidation needs to be removed to keep the temperature constant. The heat may

<sup>4</sup> $\tau$  is omitted in the following text and equations for brevity.

be further utilized in a distributed system such as a Rankine cycle power generation system, which is not discussed in this work.

## METHODOLOGY AND ASSUMPTIONS

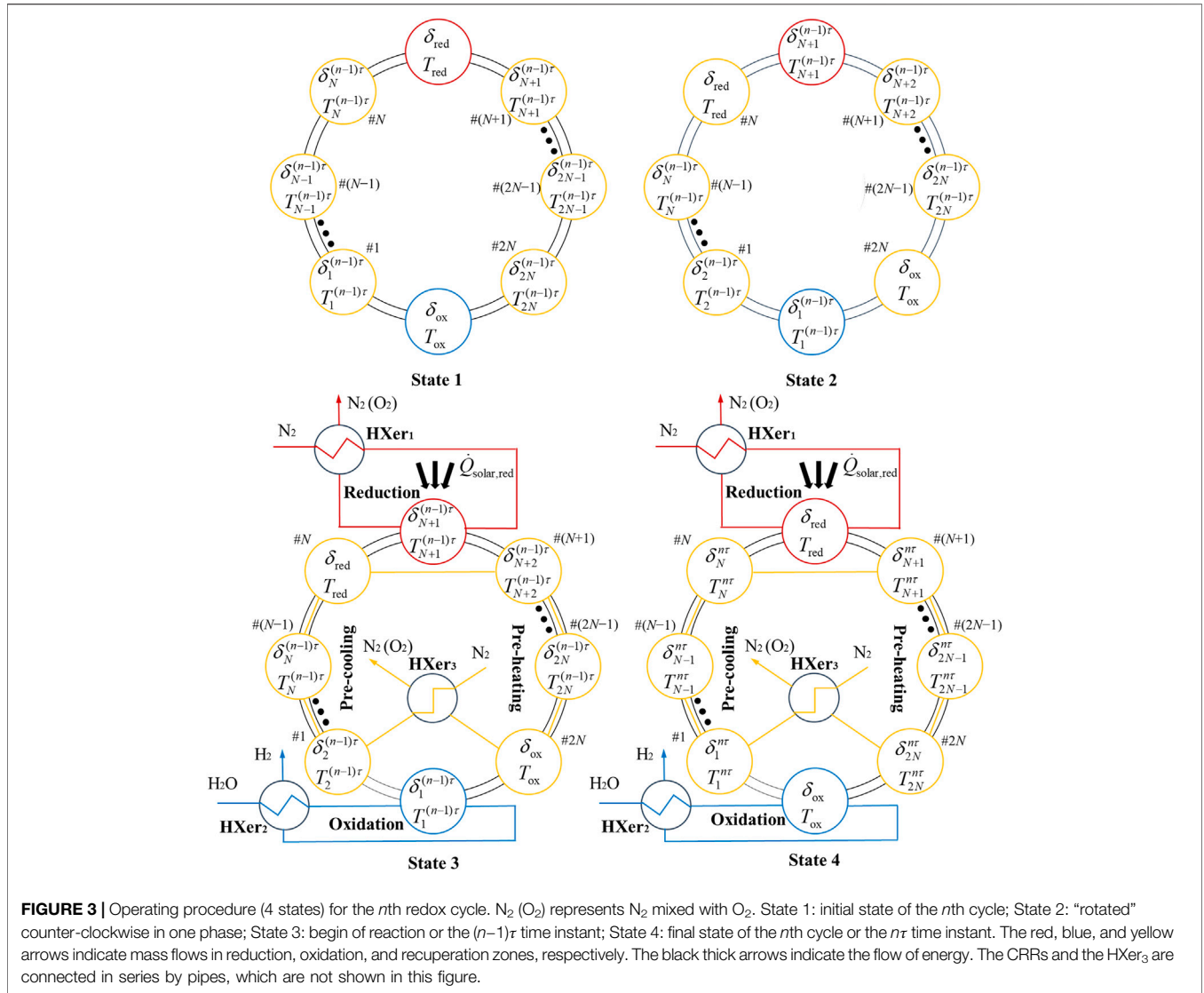
The methodology of modeling transient radiative fixed-bed reduction and cavity cascade heat recuperation is presented next. A lumped parameter model (LPM) and a linear matrix model (LMM) are, respectively, presented to describe the reducing and recuperating processes of the novel receiver-reactor redox system. For the LPM, the reduction is treated as a transient process and the numerical method is applied to solve the non-linear governing equation. For the LMM, mass and heat transfer between recuperation CRRs are expressed by a set of linear equations which is solved by matrix iteration. The main assumptions and settings are as follows:

- (1) Thermodynamic quasi-equilibrium is assumed for ceria reduction and oxidation.
- (2) Temperature difference between the RPC and sweep gases is neglected.
- (3) Lumped parameters of the RPC and gases, including temperature, relative oxygen partial pressure, non-stoichiometry,  $\text{N}_2$  flow rate, are concluded for each CRR.
- (4) The relative oxygen partial pressure  $p_{\text{O}_2}$  of the initial pure  $\text{N}_2$  flow is set to  $p_{\text{O}_2,0} = 1 \times 10^{-5}$  as a conservative estimate based on the existing industrial technologies (Häring, 2008).
- (5) The effectiveness of gas-phase heat exchanger is set to 95% according to the literature (Blank and Wu, 1994; El-Ehwany et al., 2010).
- (6) The maximum operating temperature is set to 2,000 K, as ceria will undergo a phase change at temperatures  $\geq 2,100$  K (Chueh and Haile, 1923; Bader et al., 2013).
- (7) The oxidation reaction is undergone constantly at 1,000 K.
- (8) For the LMM, the temperature of RPC (or sweep gases) in the recuperation zone varies linearly over time, namely,  $\bar{T}_\tau = \frac{1}{\tau} \int_{(n-1)\tau}^{n\tau} T dt \approx (T^{(n-1)} + T^{(n)})/2$ , and the  $\text{O}_2$  generating rate is assumed as constant.

## MATHEMATICAL MODEL

**Figure 4** shows the schematic of the system model for the reaction process in the  $n$ th cycle from the  $(n-1)\tau$  to  $n\tau$  time instant. It corresponds to the process from State 3 to 4 in **Figure 3**. The red and blue blocks represent CRRs in the reduction and oxidation zones. In the recuperation zone, the CRRs are represented in a row of yellow rectangular boxes separated into the pre-cooling and pre-heating parts. All CRRs are enclosed by a frame in the solid line as the reactor boundary. For each CRR, the initial and final thermodynamic states of ceria in the  $n$ th cycle are given correspondingly. Thick solid arrows are used to show the direction of reactions. The flows of mass and energy are represented by thin solid arrows and thick hollowed arrows,





respectively. The outermost dash frame denotes the boundary of the whole system. A steady thermodynamic state of temperature,  $T_0 = 298$  K and gauge pressure,  $p_0 = 1.013 \times 10^5$  Pa is assumed for the surroundings.

Energy conservation of the system undergoing one cycle (shown in Figure 4) is:

$$Q_{solar} = Q_{rad} + Q_{other} + Q_{gas} + Q_{quench} + Q_{reject} + Q_{fuel} \quad (1)$$

where  $Q_{solar}$  represents the total solar energy input during one cycle, including energy consumed by the reduction reaction  $Q_{solar,red}$ , and energy for the recovery of heat losses  $Q_{solar, recovery}$ . They can be expressed as:

$$Q_{solar, red} = \int_{(n-1)\tau}^{n\tau} \dot{Q}_{solar, red} dt \quad (2)$$

$$Q_{rad} = \int_{(n-1)\tau}^{n\tau} \frac{\sigma T^4}{C \times DNI} \dot{Q}_{solar, red} dt \quad (3)$$

$$Q_{solar, recovery} = Q_{other} = F(Q_{solar, red} - Q_{rad}) \quad (4)$$

where  $\dot{Q}_{solar, red}$  is the incident solar power into the reduction cavity,  $Q_{rad}$  and  $Q_{other}$  denote the radiative and other heat losses, respectively,  $\sigma$  is the Stefan–Boltzmann constant,  $\sigma = 5.67 \times 10^{-8} \text{ W m}^{-2} \text{ K}^{-4}$ ,  $C$  and DNI represent the concentration ratio and direct normal irradiation assumed equal to 3,000 and  $1,000 \text{ W m}^{-2}$ , respectively, and  $F$  is the heat loss fraction of the entire system assumed to be equal to 0.2.

$$Q_{gas} = Q_{gas, HX} + Q_{gas, red} + Q_{gas, ox} \quad (5)$$

$$Q_{quench} = m_{RPC} C_v (T_1^{(n-1)} - T_{ox}) \quad (6)$$

$$Q_{ox} = n_{H_2} \left[ \bar{h}_{H_2O}(T_{ox}) - \bar{h}_{H_2}(T_{ox}) - \frac{\Delta \bar{h}_{O_2}(\delta_1^{(n-1)}, \delta_{ox})}{2} \right] \quad (7)$$

$$Q_{reject} = Q_{ox} + n_{H_2O} [\bar{h}_{H_2O}(T_{ox}) - \bar{h}_{H_2O}(T_{ox})] - (n_{H_2O} - n_{H_2}) \frac{\Delta \bar{h}_{O_2}(\delta_{ox}, \delta_0)}{2} + \varepsilon \{ (n_{H_2O} - n_{H_2}) [\bar{h}_{H_2O}(T_{ox}) - \bar{h}_{H_2O}(T_{ox})] + n_{H_2} [\bar{h}_{H_2}(T_{ox}) - \bar{h}_{H_2}(T_{ox})] \} \quad (8)$$

$$Q_{fuel} = n_{H_2} [\bar{h}_{H_2}(T_{ox}) - \bar{h}_{H_2O}(T_{ox})] \quad (9)$$

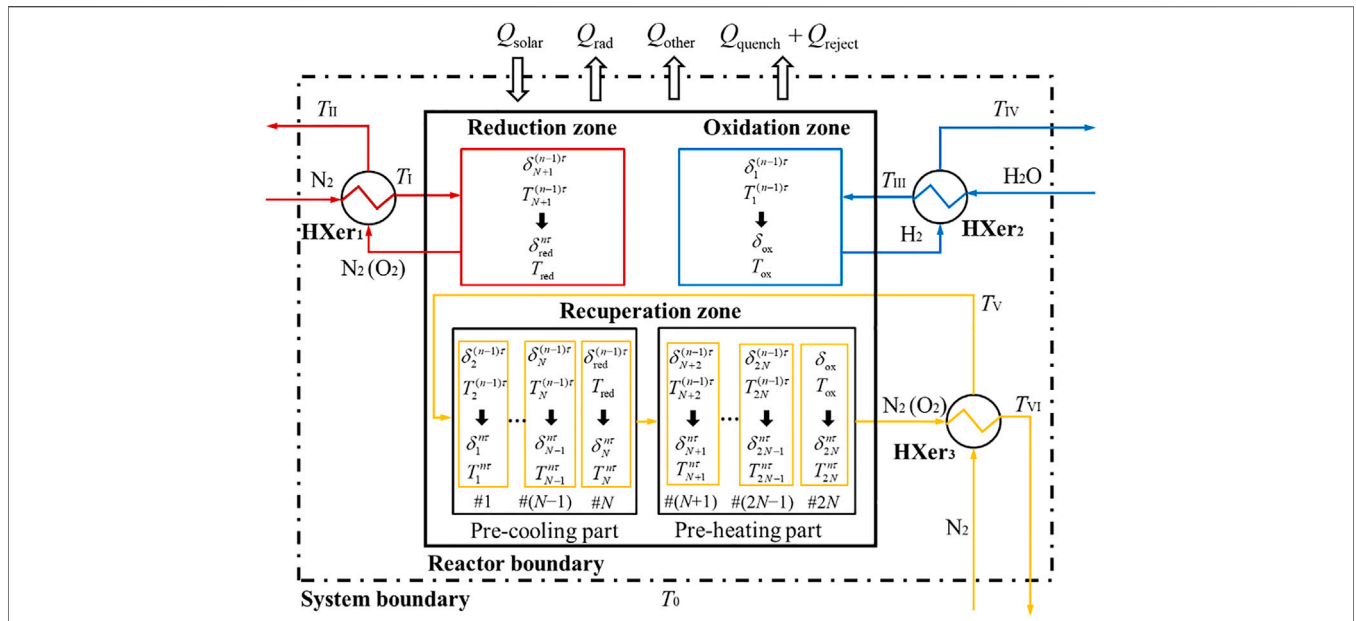


FIGURE 4 | Schematic of system model of State 3 to State 4 for the  $n$ th reaction cycle.

$$Q_{\text{gas,HX}} = \dot{m}_{\text{N}_2, \text{HX}} \tau c_{p, \text{N}_2} (1 - \varepsilon) \left( \frac{T_{\text{ox}} + T_{2N}^{(n)}}{2} - T_{\infty} \right) \quad (10)$$

$$Q_{\text{gas,red}} = \int_{(n-1)\tau}^{n\tau} \left[ \dot{m}_{\text{N}_2, \text{red}} c_{p, \text{N}_2} (1 - \varepsilon) (T - T_{\infty}) + \frac{m_{\text{RPC}} M_{\text{O}_2} c_{p, \text{O}_2}}{2M_{\text{RPC}}} \frac{d\delta}{dt} (T_{\infty} - T) \right] dt \quad (11)$$

$$Q_{\text{gas,ox}} = (1 - \varepsilon) \left\{ n_{\text{H}_2} [\bar{h}_{\text{H}_2} (T_{\text{ox}}) - \bar{h}_{\text{H}_2} (T_{\infty})] + (n_{\text{H}_2\text{O}} - n_{\text{H}_2}) \times [\bar{h}_{\text{H}_2\text{O}} (T_{\text{ox}}) - \bar{h}_{\text{H}_2\text{O}} (T_{\infty})] \right\} \quad (12)$$

where  $Q_{\text{gas}}$  is the gas-phase heat recovery loss equal to the sum of the heat losses during heat exchanging, reducing, and oxidizing processes,  $Q_{\text{gas,HX}}$ ,  $Q_{\text{gas,red}}$ , and  $Q_{\text{gas,ox}}$ , respectively, which are calculated using Eqs. 10–12.  $Q_{\text{quench}}$  in Eq. 6 is the quenching heat loss for rapidly cooling ceria from  $T_1^{(n-1)}$  to  $T_{\text{ox}}$  before oxidation. Using Eq. 7 to calculate the heat released during oxidation.  $n_{\text{H}_2\text{O}}$  and  $n_{\text{H}_2}$  are the total amounts of  $\text{H}_2\text{O}$  supplied and  $\text{H}_2$  produced in one redox cycle, respectively.  $Q_{\text{ox}}$  can be partially used for re-heating inlet water steam up to  $T_{\text{ox}}$ . The redundant heat of  $Q_{\text{ox}}$  is assumed to be rejected completely as calculated by Eq. 8.  $\varepsilon$  is the heat recovery effectiveness of gas-phase heat exchanger.  $Q_{\text{fuel}}$  in Eq. 9 is the thermal energy stored in the product of  $\text{H}_2$ . The reference temperature is  $T_{\text{ref}} = 1500$  K and the reference pressure is  $p_{\text{ref}} = 1.013 \times 10^5$  Pa. Physical properties of the sweeping gases and non-stoichiometric  $\text{CeO}_2$  including the specific heat at constant pressure ( $c_p$ ) and constant volume ( $c_v$ ) refer to  $T_{\text{ref}}$  and  $p_{\text{ref}}$ .

### Reduction Reaction

The governing equations of the LPM for simulating the non-linear solar reduction process are:

$$m_{\text{RPC}} c_v dT + \frac{m_{\text{RPC}}}{2M_{\text{RPC}}} d\delta \Delta \bar{h}_{\text{O}_2} = \left( 1 - \frac{\sigma T^4}{C \times \text{DNI}} \right) \dot{Q}_{\text{solar,red}} dt + \dot{m}_{\text{N}_2, \text{red}} c_{p, \text{N}_2} (1 - \varepsilon) (T_{\infty} - T) dt + \frac{m_{\text{RPC}} M_{\text{O}_2} c_{p, \text{O}_2}}{2M_{\text{RPC}}} d\delta (T_{\infty} - T) \quad (13)$$

The implicit Euler time integration scheme is applied. Thus,

$$T^{(m)} = T^{(m-1)} + \left( 1 - \frac{\sigma T^{(m)4}}{C \times \text{DNI}} \right) \frac{\dot{Q}_{\text{solar,red}} \Delta \tau}{m_{\text{RPC}} c_v} - \frac{\delta^{(m)} - \delta^{(m-1)}}{2M_{\text{RPC}} c_v} \Delta \bar{h}_{\text{O}_2} (\delta^{(m-1)}, \delta^{(m)}) + \left[ \frac{\dot{m}_{\text{N}_2, \text{red}} c_{p, \text{N}_2} (1 - \varepsilon) \Delta \tau}{m_{\text{RPC}} c_v} + \frac{M_{\text{O}_2} c_{p, \text{O}_2}}{2M_{\text{RPC}} c_v} (\delta^{(m)} - \delta^{(m-1)}) \right] (T_{\infty} - T^{(m)}) \quad (14)$$

$$\Delta G_{\text{red}} = \Delta H_{\text{red}}^{\circ} (\delta^{(m)}) - T_{\text{red}} \Delta S_{\text{red}}^{\circ} (\delta^{(m)}) + RT_{\text{red}} \ln \left( \frac{p_{\text{O}_2}^{(m)}}{p_{\text{ref}}} \right) = 0 \quad (15)$$

$$p_{\text{O}_2}^{(m)} = \frac{r_{\text{O}_2}}{r_{\text{N}_2} + r_{\text{O}_2}} + p_{\text{O}_2,0} \frac{m_{\text{RPC}} (\delta^{(m)} - \delta^{(m-1)})}{2M_{\text{RPC}} \Delta \tau} = \frac{\dot{m}_{\text{N}_2, \text{red}}}{M_{\text{N}_2}} + \frac{m_{\text{RPC}} (\delta^{(m)} - \delta^{(m-1)})}{2M_{\text{RPC}} \Delta \tau} + p_{\text{O}_2,0} \quad (16)$$

$\delta$  at the end of each time step is obtained by solving Eq. 15 using experimental data of non-stoichiometric cerium dioxide at thermodynamic equilibrium (Panlener et al., 1975).  $\Delta H_{\text{red}}^{\circ}$  and  $\Delta S_{\text{red}}^{\circ}$  are the standard reaction enthalpy and entropy of ceria reduction per mole of the released  $\text{O}_2$ , respectively. A species

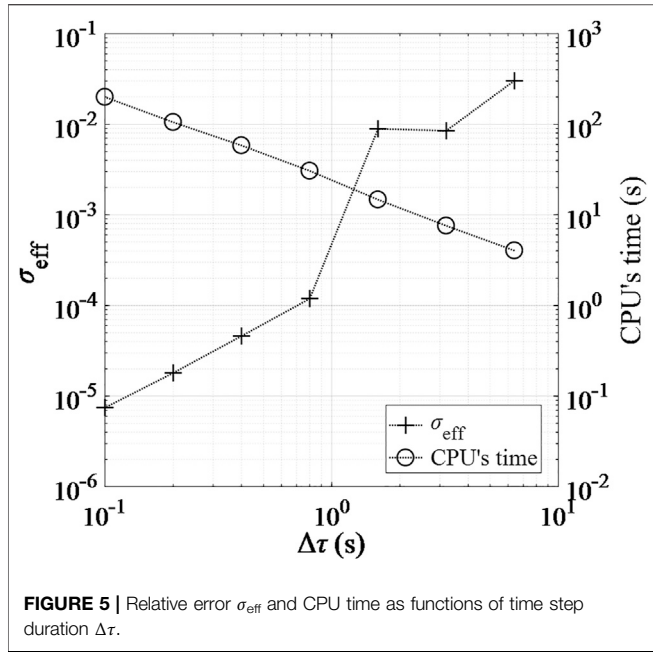


**FIGURE 5** | Relative error  $\sigma_{\text{eff}}$  and CPU time as functions of time step duration  $\Delta\tau$ .

balance relates the pressure of oxygen at the outlet of the reactor,  $p_{\text{O}_2}$ , to the rate at which oxygen is generated,  $r_{\text{O}_2}$ , by Eq. 16.  $\dot{m}_{\text{N}_2, \text{red}}$  is continuously adjusted throughout the reducing process to approximate a constant  $p_{\text{O}_2}$ . A relaxation factor  $\chi$  is used to smoothen the iteration of  $\dot{m}_{\text{N}_2, \text{red}}$  due to its high sensitivity to the results, namely  $\dot{m}_{\text{N}_2, \text{red}} = \chi \dot{m}_{\text{N}_2, \text{red}}^{(m)} + (1 - \chi) \dot{m}_{\text{N}_2, \text{red}}^{(m-1)}$ . **Figure 5** shows the computational accuracy and time as functions of the time step  $\Delta\tau$ . The relative error  $\sigma_{\text{eff}}$  is defined as  $\sigma_{\text{eff}} = |\eta_{\text{th}} - \eta_{\text{th,ref}}| / \eta_{\text{th,ref}}$ , where  $\eta_{\text{th,ref}}$  is calculated for a reference  $\Delta\tau = 0.01$  s. Based on **Figure 5**,  $\Delta\tau$  is set to 0.1 s to ensure relatively higher accuracy.

### Heat Recuperation

For modeling the recuperating process, the LMM is established. The energy-balance equation for CRRs in the recuperation zone from State 3 to State 4 in a redox cycle is as follows:

$$\begin{aligned}
 & m_{\text{RPC}} c_v (T_i^{(n)} - T_{i+1}^{(n-1)}) + \frac{m_{\text{RPC}}}{M_{\text{RPC}}} \frac{\delta_i^{(n)} - \delta_{i+1}^{(n-1)}}{2} \Delta \bar{h}_{\text{O}_2} (\delta_{i+1}^{(n-1)}, \delta_i^{(n)}) \\
 & = \dot{m}_{\text{N}_2, \text{HX}} c_{p, \text{N}_2} \tau \left[ \left( 1 + \frac{M_{\text{O}_2} c_{p, \text{O}_2}}{M_{\text{N}_2} c_{p, \text{N}_2}} \frac{p_{\text{O}_2, i-1}^{(n)}}{p_{\text{N}_2, i-1}^{(n)}} \right) \left( \frac{T_{i-1}^{(n)} + T_i^{(n-1)}}{2} - T_{\infty} \right) \right. \\
 & \quad \left. - \left( 1 + \frac{M_{\text{O}_2} c_{p, \text{O}_2}}{M_{\text{N}_2} c_{p, \text{N}_2}} \frac{p_{\text{O}_2, i}^{(n)}}{p_{\text{N}_2, i}^{(n)}} \right) \left( \frac{T_i^{(n)} + T_{i+1}^{(n-1)}}{2} - T_{\infty} \right) \right] \\
 & (1 < i \leq 2N) \tag{17}
 \end{aligned}$$

where the subscript  $i$  represents the CRR position of the recuperation zone and the superscript  $n$  represents the  $n$ th redox cycle. As shown in **Figure 3**,  $X_i^{(n)}$  and  $X_{i+1}^{(n-1)}$  ( $X$ :  $T$ ,  $\delta$ ) correspond to thermodynamic parameter values of RPC in  $\#i$  CRR position at State 4 and State 3 of the  $n$ th redox cycle, respectively. For  $\#N$  and  $\#2N$  positions,  $X_{i+1}^{(n-1)}$  corresponds to  $T_{\text{red}}$ ,  $\delta_{\text{red}}$ , and  $T_{\text{ox}}$ ,  $\delta_{\text{ox}}$ , respectively.

The LHS of Eq. 17 represents the change in internal energy of RPC material corresponding to  $\#i$  position, and the RHS is the net amount of thermal energy input (or output) by  $\text{N}_2$  from State 3 to State 4. For  $\#1$  position of the recuperation zone, the heat loss of gas-phase heat recovery should be considered, and the modified equation is:

$$\begin{aligned}
 & m_{\text{RPC}} c_v (T_1^{(n)} - T_2^{(n-1)}) + \frac{m_{\text{RPC}}}{M_{\text{RPC}}} \frac{\delta_1^{(n)} - \delta_2^{(n-1)}}{2} \Delta \bar{h}_{\text{O}_2} (\delta_2^{(n-1)}, \delta_1^{(n)}) \\
 & = \dot{m}_{\text{N}_2, \text{HX}} c_{p, \text{N}_2} \tau \left[ \varepsilon \left( \frac{T_{2\text{N}}^{(n)} + T_{\text{ox}}}{2} - T_{\infty} \right) \right. \\
 & \quad \left. - \left( 1 + \frac{M_{\text{O}_2} c_{p, \text{O}_2}}{M_{\text{N}_2} c_{p, \text{N}_2}} \frac{p_{\text{O}_2, 1}^{(n)}}{p_{\text{N}_2, 1}^{(n)}} \right) \left( \frac{T_1^{(n)} + T_2^{(n-1)}}{2} - T_{\infty} \right) \right] \tag{18}
 \end{aligned}$$

where  $\varepsilon$  is gas-phase heat recovery effectiveness,  $p_{\text{O}_2, i}^{(n)}$  is determined by the mass flow rate of  $\text{N}_2$  and  $\text{O}_2$ ,  $\dot{m}_{\text{N}_2}$  and  $\dot{m}_{\text{O}_2, i}^{(n)}$  respectively,  $\dot{m}_{\text{N}_2}$  and  $\dot{m}_{\text{O}_2, i}^{(n)}$  can be calculated as:

$$\dot{m}_{\text{O}_2, i}^{(n)} = \frac{\left[ \delta_1^{(n)} - \delta_{i+1}^{(n-1)} + \sum_{j=2}^{i>1} (\delta_j^{(n)} - \delta_j^{(n-1)}) \right] m_{\text{RPC}} M_{\text{O}_2}}{2 M_{\text{RPC}} \tau} \tag{19}$$

$$\begin{aligned}
 p_{\text{O}_2, i}^{(n)} & = \frac{\frac{\dot{m}_{\text{O}_2, i}^{(n)}}{M_{\text{O}_2}}}{\frac{\dot{m}_{\text{N}_2, \text{HX}}}{M_{\text{N}_2}} + \frac{\dot{m}_{\text{O}_2, i}^{(n)}}{M_{\text{O}_2}}} + p_{\text{O}_2, 0} \\
 & = \frac{\delta_1^{(n)} - \delta_{i+1}^{(n-1)} + \sum_{j=2}^{i>1} (\delta_j^{(n)} - \delta_j^{(n-1)})}{2\beta \gamma_{\text{N}_2}^{\text{RPC}} + \delta_1^{(n)} - \delta_{i+1}^{(n-1)} + \sum_{j=2}^{i>1} (\delta_j^{(n)} - \delta_j^{(n-1)})} + p_{\text{O}_2, 0} \tag{20}
 \end{aligned}$$

where  $\beta = \frac{\dot{m}_{\text{N}_2, \text{HX}} c_{p, \text{N}_2} \tau}{m_{\text{RPC}} c_v}$  and  $\gamma_{\text{N}_2}^{\text{RPC}} = \frac{M_{\text{RPC}} c_v}{M_{\text{N}_2} c_{p, \text{N}_2}}$ .

A non-dimensional parameter  $\beta$ , defined as the ratio of the speed of thermal flow,  $v_{\text{TF}} = \dot{m}_{\text{N}_2, \text{HX}} c_{p, \text{N}_2}$ , to the effective rotating speed of CRR-disk,  $v_{\text{rotating}} = m_{\text{RPC}} c_v / \tau$ , is used. Three special cases,  $\beta = 0$ , 1 and  $\infty$ , are discussed under simplified conditions: perfect gas-phase heat recovery and no chemical reaction.

**Figure 6** shows the steady-state temperature distributions of the CRR array, containing a reduction CRR, an oxidation CRR, and six recuperation CRRs, at the end of a cycle when reaching a steady running condition. For  $0 < \beta < 1$ , the solid-phase heat recovery in the recuperation zone is insufficient, and the heat recovery efficiency can be improved by increasing  $\beta$ . The highest heat recovery efficiency,  $\eta_{\text{recovery}} = (T_4 - T_{\text{ox}}) / (T_{\text{red}} - T_{\text{ox}})$ , is found at  $\beta = 1$ , where the final temperature distributions of the pre-heating and pre-cooling CRRs are identical (**Figure 6B**). Further increase of  $\beta$  leads to a detrimental effect on solid-phase heat recovery. Because the temperature of CRR in  $\#3$  drops below 1675 K when  $\beta > 1$ , the CRR in  $\#4$  will be cooled. Finally, the temperatures of all CRRs in the recuperation zone approach the same value of 1450 K when  $\beta = \infty$ . In this study,  $\beta$  is set to 1.

Besides, as given in Eq. 21,  $\delta$  in each recuperation CRR is determined by  $p_{\text{O}_2}$ ,  $T$ , and other constraints. During the

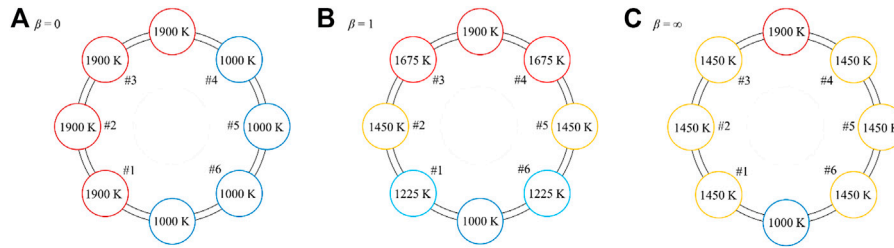


**FIGURE 6** | Steady-state temperature distributions in the CRR array at the end of a cycle for **(A)**  $\beta = 0$ , **(B)**  $\beta = 1$ , and **(C)**  $\beta = \infty$ .

change from State 1 to State 2, the recuperation CRR containing  $\text{CeO}_{2-\delta}$  with  $\delta_{i+1}^{(n-1)}$  is shifted counter-clockwise from  $\#(i+1)$  to  $\#i$  position as shown in **Figure 3**. Then, the CRR's thermodynamic state moves from  $(p_{\text{O}_2,i+1}^{(n-1)}, T_{i+1}^{(n-1)})$  to a new state,  $(p_{\text{O}_2,i}^{(n)}, T_i^{(n)})$  during the change from State 3 to State 4. For the pre-heating CRRs, namely  $(N+1) \leq i \leq 2N$ ,  $\delta_i^{(n)}$  is solely determined by  $(p_{\text{O}_2,i}^{(n)}, T_i^{(n)})$ . For the pre-cooling CRRs, namely  $1 \leq i \leq N$ , two possibilities should be discussed. The first possible condition is that  $\delta$  determined by the new thermodynamic state  $(p_{\text{O}_2,i}^{(n)}, T_i^{(n)})$  is larger than the previous non-stoichiometry  $\delta_{i+1}^{(n-1)}$ . According to the assumption of thermodynamic quasi-equilibrium, a further reduction can occur and  $\delta_i^{(n)}$  is obtained by solving  $f(p_{\text{O}_2,i}^{(n)}, T_i^{(n)}, \delta_i^{(n)}) = 0$  which is similar to **Eq. 15**. The second possible condition is  $\delta < \delta_{i+1}^{(n-1)}$ , and a re-oxidation should occur. However, this is inhibited due to the absence of  $\text{O}_2$  in pure  $\text{N}_2$  flows ( $p_{\text{O}_2,0} = 1 \times 10^{-5}$ ). Because less  $\text{O}_2$  can be regained by the ceria, the reaction extent is too small. It is found that the decrement of  $\Delta\delta$  is orders of magnitude smaller than  $\delta_{\text{red}}$ . Therefore,  $\delta_i^{(n)}$  is assumed to be equal to  $\delta_{i+1}^{(n-1)}$  in the second condition.

$$\delta_i^{(n)} = \begin{cases} \max[\delta_{i+1}^{(n-1)}, f(p_{\text{O}_2,i}^{(n)}, T_i^{(n)})], & 1 \leq i \leq N \\ f(p_{\text{O}_2,i}^{(n)}, T_i^{(n)}), & N + 1 \leq i \leq 2N \end{cases} \quad (21)$$

**Equations 13** and **14** can be written in a matrix form as:

$$\mathbf{A} \cdot \mathbf{T}^{(n)} = \mathbf{B} \cdot \mathbf{T}_{\text{shift}}^{(n-1)} + \mathbf{V}_{\text{trans}} - \mathbf{V}_{\text{chem}} \quad (22)$$

where

$$\mathbf{A} = \begin{bmatrix} 2 + \beta(1 + \xi_1^{(n)}) & 0 & \dots & -\varepsilon\beta \\ -\beta(1 + \xi_1^{(n)}) & 2 + \beta(1 + \xi_2^{(n)}) & \dots & 0 \\ \vdots & \vdots & \ddots & \vdots \\ 0 & \dots & -\beta(1 + \xi_{2N-1}^{(n)}) & 2 + \beta(1 + \xi_{2N}^{(n)}) \end{bmatrix}$$

$$\mathbf{B} = \begin{bmatrix} \varepsilon\beta & 2 - \beta(1 + \xi_1^{(n)}) & \dots & 0 \\ 0 & \beta(1 + \xi_1^{(n)}) & 2 - \beta(1 + \xi_2^{(n)}) & \dots \\ \vdots & \vdots & \vdots & \vdots \\ 2 - \beta(1 + \xi_{2N}^{(n)}) & \dots & 0 & \beta(1 + \xi_{2N-1}^{(n)}) \end{bmatrix}$$

$$\mathbf{V}_{\text{trans}} = \begin{bmatrix} 2\beta(1 + \xi_1^{(n)} - \varepsilon)T_{\infty} \\ 2\beta(\xi_2^{(n)} - \xi_1^{(n)})T_{\infty} \\ \vdots \\ 2\beta(\xi_{2N}^{(n)} - \xi_{2N-1}^{(n)})T_{\infty} \end{bmatrix}, \mathbf{V}_{\text{chem}}$$

$$= \begin{bmatrix} \frac{\delta_1^{(n)} - \delta_2^{(n-1)}}{M_{\text{RPC}}c_v} \Delta \bar{h}_{\text{O}_2}(\delta_2^{(n-1)}, \delta_1^{(n)}) \\ \frac{\delta_2^{(n)} - \delta_3^{(n-1)}}{M_{\text{RPC}}c_v} \Delta \bar{h}_{\text{O}_2}(\delta_3^{(n-1)}, \delta_2^{(n)}) \\ \vdots \\ \frac{\delta_{2N}^{(n)} - \delta_{\text{ox}}}{M_{\text{RPC}}c_v} \Delta \bar{h}_{\text{O}_2}(\delta_{\text{ox}}, \delta_{2N}^{(n)}) \end{bmatrix}$$

$$\mathbf{T}^{(n)} = \begin{bmatrix} T_1^{(n)} \\ T_2^{(n)} \\ \vdots \\ T_{2N}^{(n)} \end{bmatrix}, \mathbf{T}_{\text{shift}}^{(n-1)} = \begin{bmatrix} T_{\text{ox}} \\ T_2^{(n-1)} \\ \vdots \\ T_{2N}^{(n-1)} \end{bmatrix}, \xi_i^{(n)} = \gamma_{\text{N}_2}^{\text{O}_2} \frac{p_{\text{O}_2,i}^{(n)}}{p_{\text{N}_2,i}^{(n)}}, \text{ and } \gamma_{\text{N}_2}^{\text{O}_2} = \frac{M_{\text{O}_2}c_{p,\text{O}_2}}{M_{\text{N}_2}c_{p,\text{N}_2}}$$

Vectors  $\mathbf{T}^{(n)}$  and  $\mathbf{T}_{\text{shift}}^{(n-1)}$  contain the temperatures of  $2N$  recuperation CRRs with respect to State 4 and State 3 in the  $n$ th cycle.  $\mathbf{V}_{\text{trans}}$  and  $\mathbf{V}_{\text{chem}}$  are vectors containing the themes related to the item of heat losses via gas-phase transport and the item of chemical enthalpy in the  $n$ th cycle. Finally, steady operation can be achieved as the iteration approaches a convergence solution, namely,  $\lim_{n \rightarrow \infty} \mathbf{T}^{(n)} = \mathbf{T}$ . The convergence criterion is:

$$\sqrt{\frac{1}{2N} \sum_1^{2N} \left( \frac{T_i^{(n)} - T_i^{(n-1)}}{T_i^{(n-1)}} \right)^2} < 10^{-6} \quad (23)$$

### Oxidation Reaction

The process of oxidation involves two synchronous reactions: ceria re-oxidation and water splitting (WS). Similar to the reduction modeling, the lumped transient method is applied with the assumption of quasi thermodynamical equilibrium for each time step, namely  $\Delta G_{\text{ox}} = 0$ . The expression is given by :



**TABLE 1** | Baseline model parameters.

Parameter	Value	Unit
Solar power input to the reduction reaction, $\dot{Q}_{\text{solar,red}}$	1,000	W
Flux concentration ratio at the receiver–reactor aperture, $C$	3,000	–
Direct normal irradiance, DNI	1,000	W m <sup>-2</sup>
Oxidation temperature, $T_{\text{ox}}$	1,000	K
Reduction temperature, $T_{\text{red}}$	1900	K
Ambient temperature, $T_{\infty}$	298	K
Relative oxygen partial pressure of reduction, $p_{\text{O}_2}$	0.01	–
CRR numbers, $N_{\text{cav}}$	Reduction zone, $N_{\text{red}}$	1
	Oxidation zone, $N_{\text{ox}}$	1
	Recuperation zone, $2N$	10
Gas-phase heat recovery effectiveness, $\epsilon$	Pre-cooling part, $N$	10
	Pre-heating part, $N$	10
Loss factor, $F$	0.95	–
	0.2	–

$$\Delta G_{\text{ox}} = [\Delta H_{\text{WS}}^{\circ} - T_{\text{ox}} \Delta S_{\text{WS}}^{\circ}] - \frac{\Delta H_{\text{red}}^{\circ}(\delta^{(m)}) - T_{\text{ox}} \Delta S_{\text{red}}^{\circ}(\delta^{(m)})}{2} + RT_{\text{ox}} \ln \left( \frac{r_{\text{H}_2}^{(m)}}{r_{\text{H}_2\text{O}}^{(m)} - r_{\text{H}_2}^{(m)}} \right) = 0 \quad (24)$$

where  $\Delta H_{\text{WS}}^{\circ}$  and  $\Delta S_{\text{WS}}^{\circ}$  are the standard reaction enthalpy and entropy for water splitting per mole of the released H<sub>2</sub>.  $r_{\text{H}_2\text{O}}$  and  $r_{\text{H}_2}$  are the flow rate of water at inlet and the generation rate of H<sub>2</sub>, respectively. Here, the  $r_{\text{H}_2\text{O}}$  is set equal to  $\frac{n_{\text{H}_2\text{O}}}{\tau}$ . To re-oxidize ceria as much as possible,  $n_{\text{H}_2\text{O}}$  is set to the maximum value calculated by Eq. 25, in which case the generated chemical heat is completely utilized for heating water. In addition, the connection of  $r_{\text{H}_2}$  and  $\delta$  is given by Eq. 26.

$$n_{\text{H}_2\text{O}} = \frac{m_{\text{RPC}}(\delta_{\text{red}} - \delta_0)}{M_{\text{RPC}}(1 - \epsilon)[\bar{h}_{\text{H}_2\text{O}}(T_{\infty}) - \bar{h}_{\text{H}_2\text{O}}(T_{\text{ox}})]} \left\{ \epsilon[\bar{h}_{\text{H}_2}(T_{\infty}) - \bar{h}_{\text{H}_2\text{O}}(T_{\infty})] + (1 - \epsilon)[\bar{h}_{\text{H}_2}(T_{\text{ox}}) - \bar{h}_{\text{H}_2\text{O}}(T_{\text{ox}})] - \frac{\Delta \bar{h}_{\text{O}_2}(\delta_1^{(n-1)}, \delta_0)}{2} \right\} \quad (25)$$

$$\delta = \delta_{\text{red}} - \frac{M_{\text{RPC}}}{m_{\text{RPC}}} \int_0^t r_{\text{H}_2} dt \quad (26)$$

In the present work, we propose an effective recuperation system to enhance the solid-phase heat exchange. System performance is characterized by the heat recovery effectiveness  $\epsilon_{\text{solid}}$  defined as the ratio of the recovered thermal energy  $Q_{\text{rec,solid}}$  to the thermal enthalpy change of RPC during the redox cycle, and solar-to-fuel efficiency of the overall system defined as the total amount of thermal energy output of hydrogen divided by the concentrated solar energy input:

$$Q_{\text{rec,solid}} = m_{\text{RPC}} c_v (T_{N+1} - T_{\text{ox}}) \quad (27)$$

$$\epsilon_{\text{solid}} = \frac{Q_{\text{rec,solid}}}{m_{\text{RPC}} c_v (T_{\text{red}} - T_{\text{ox}})} \quad (28)$$

$$\eta_{\text{th}} = \frac{Q_{\text{fuel}}}{Q_{\text{solar}}} \quad (29)$$

## RESULTS AND DISCUSSION

In this section, we first present the verification of the described mathematical model and its assumptions. Then, we present the performance of the proposed receiver–reactor array. Finally, we show the results of a sensitivity study of the thermal-to-chemical efficiency as functions of the concentration ratio  $C$ , the number of CRRs in the pre-cooling or pre-heating part,  $N$ , the gas-phase heat recovery effectiveness  $\epsilon$ , the reduction temperature,  $T_{\text{red}}$ , and the relative oxygen partial pressure,  $p_{\text{O}_2}$ . The baseline model parameters used in this study are listed in Table 1.

### Model Verification

The present model is verified by comparing its selected predictions with the numerical and experimental results obtained by Venstrom et al. (2015) for the reduction reaction of a fixed-bed of ceria. Firstly, we compare the O<sub>2</sub> production rate,  $r_{\text{O}_2}$ . The same operating conditions are applied: (1) the ceria is heated from 1,013 to 1,748 K at a rate of 100 K min<sup>-1</sup> and then it kept isothermal for 4 min; (2) N<sub>2</sub> sweep gas flow is constant at 900 mL min<sup>-1</sup> g<sub>ceria</sub><sup>-1</sup>; (3) the mass of ceria is 1.0245 g; and (4) the initial  $\delta$  is assumed to be equal to 10<sup>-5</sup>. Figure 7 shows the O<sub>2</sub> production rates during the reduction reaction of fixed-bed ceria predicted by the two models. A good agreement has been found, indicating that the present model provides adequate accuracy to model the transient thermal reduction reaction of fix-bed ceria. Secondly, experiments were conducted by Venstrom et al. (2015) to test a horizontal reactor under isothermal conditions in an infrared (IR) imaging furnace. The reactor comprised a packed-bed of porous ceria particles. The N<sub>2</sub> sweep gas flows were controlled with the high accuracy mass flow controllers.  $r_{\text{O}_2}$  was measured in real-time using a Raman laser gas analyzer. The experimental data of  $r_{\text{O}_2}$  are taken to compare with the results predicted from the present model, which is shown in Figure 8. The two sets of data correspond to N<sub>2</sub> sweep gas flows of 150 and 300 mL min<sup>-1</sup> g<sup>-1</sup> at a constant reduction temperature  $T_{\text{red}} = 1773$  K. The shaded region in the plots indicates the range of rates predicted by the model due to the uncertainty in the initial  $\delta$  (0.021 ± 0.002). Figure 8 shows a satisfactory agreement of  $r_{\text{O}_2}$  predicted by the present model and measured by Venstrom et al. (2015).

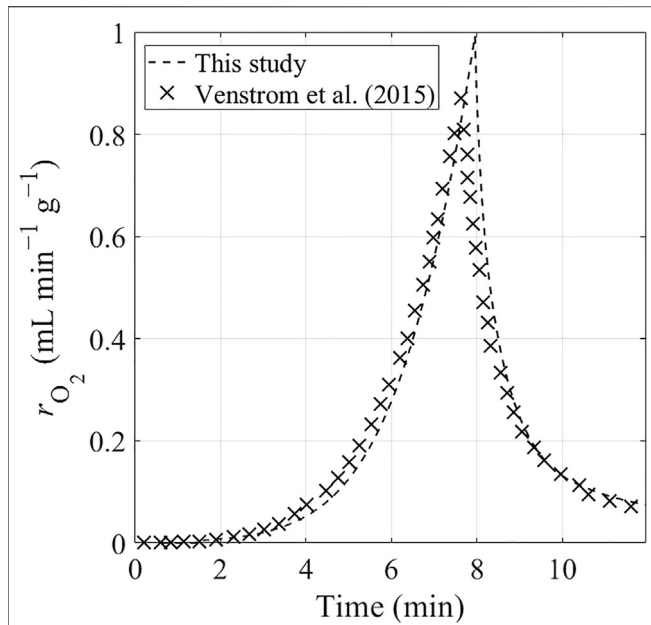


**FIGURE 7** | Transient O<sub>2</sub> production rate from reduction reaction of fixed-bed ceria predicted by two numerical models: the model developed by Venstrom et al. (2015) (represented by the crosses) and the present model (represented by the dashed curves). The reduction reaction is operated under an increasing temperature and a constant N<sub>2</sub> flow.

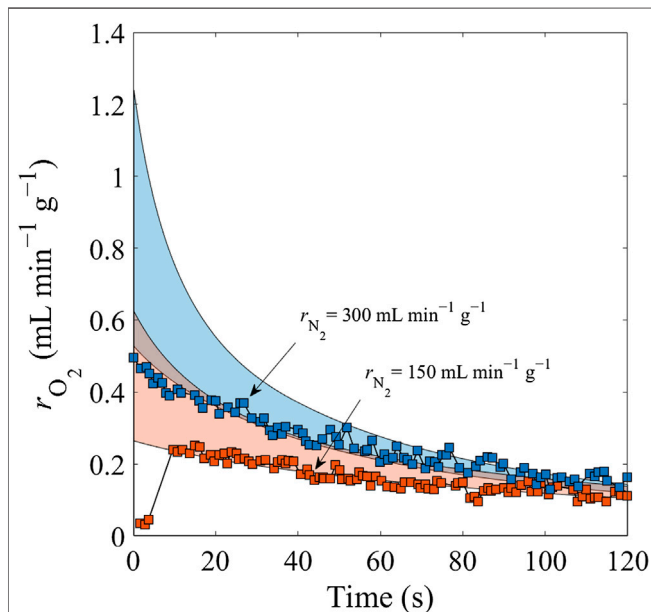


**FIGURE 8** | Comparison of predicted (color areas) and measured (squares) data for N<sub>2</sub> sweep gas flows of 150 mL min<sup>-1</sup> g<sup>-1</sup> (orange) and 300 mL min<sup>-1</sup> g<sup>-1</sup> (blue) at a constant reduction temperature  $T_{red} = 1,773$  K.

In addition, according to the second law of thermodynamics, Gibbs’s criterion should be followed at any time for chemical processes to spontaneously take place at specified thermodynamical conditions (Li et al., 2018a; Li et al., 2018b). In

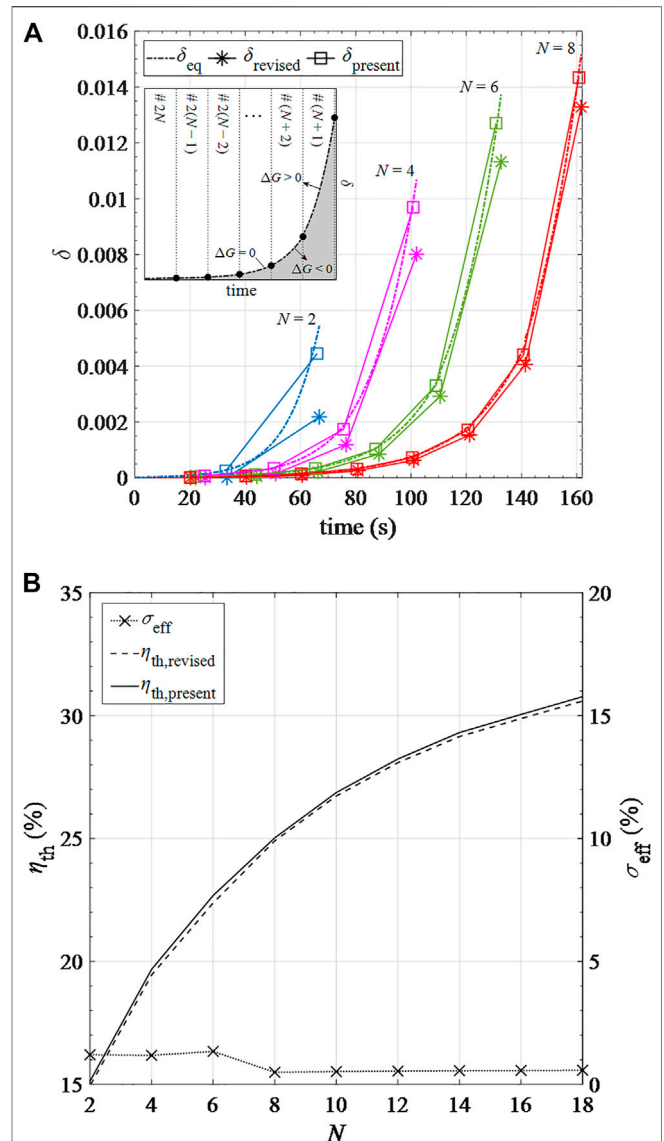


**FIGURE 9** | Results of (A)  $\delta$  over time based on the present model ( $\delta_{present}$ ), the revised model ( $\delta_{revised}$ ) and the equilibrium assumption ( $\delta_{eq}$ ) in different pre-heating cavity numbers; (B) solar-to-fuel efficiencies based on the present ( $\eta_{present}$ ) and revised ( $\eta_{revised}$ ) models and their relative errors  $\sigma_{eff}$  in different pre-heating cavity numbers.

this study, we made an important assumption that for the recuperation step, the transient change of  $\delta$  for each pre-heating cavity is linear during a cycle. Chemical reactions are assumed at equilibrium states at the beginning and the end of each cycle, namely  $\Delta G = 0$ . As shown in the inset of Figure 9A, it takes  $N$  cycles to complete the pre-heating process for the cavity to move from # $2N$  to # $(N+1)$  position. The maximum  $\delta$  at each temperature to reach thermodynamic equilibrium,  $\delta_{eq}$ , is calculated and plotted in Figure 9 (the dashed curve in the inserted figure). The curve of  $\delta_{eq}$  separates the full area into two regions: the gray region,  $\Delta G < 0$ , and the white region,  $\Delta G > 0$ . To meet the Gibbs’ criterion,  $\delta$  should always be below  $\delta_{eq}$ , namely in the gray region. Figure 9A shows that the values of  $\delta$  under the assumption of linear change of  $\delta$  in the

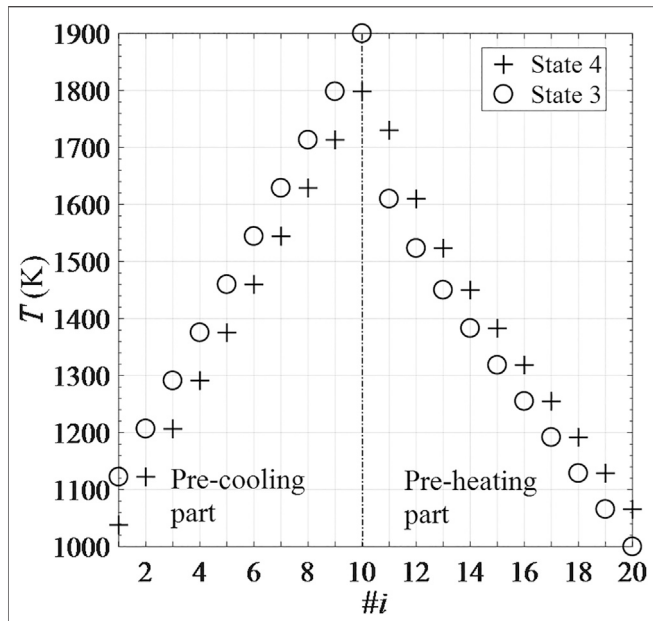


**FIGURE 10 |** Temperature distribution of 20 recuperation CRRs corresponding to State 3 and State 4 of one cycle under steady conditions.

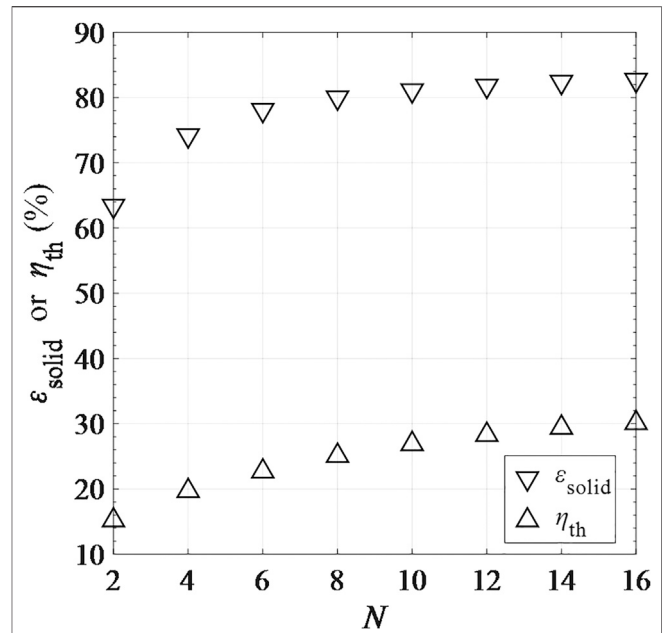


**FIGURE 12 |** Solid-phase heat recovery effectiveness  $\epsilon_{\text{solid}}$  and total solar-to-fuel efficiency  $\eta_{\text{th}}$  as functions of number of CRRs in one side of the recuperation zone (the pre-cooling or pre-heating part),  $N$ .

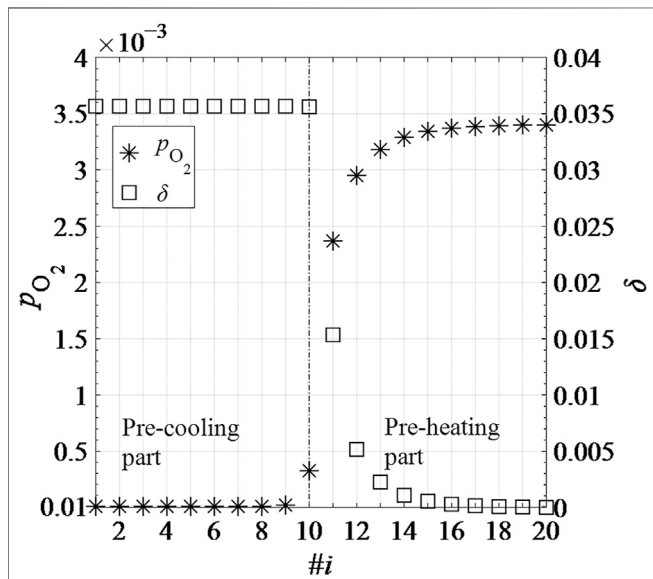


**FIGURE 11 |** Thermodynamic parameters  $\delta$  and  $p_{\text{O}_2}$  as a function of recuperation CRR position ( $\#i$ ) at the end of a cycle under steady conditions.

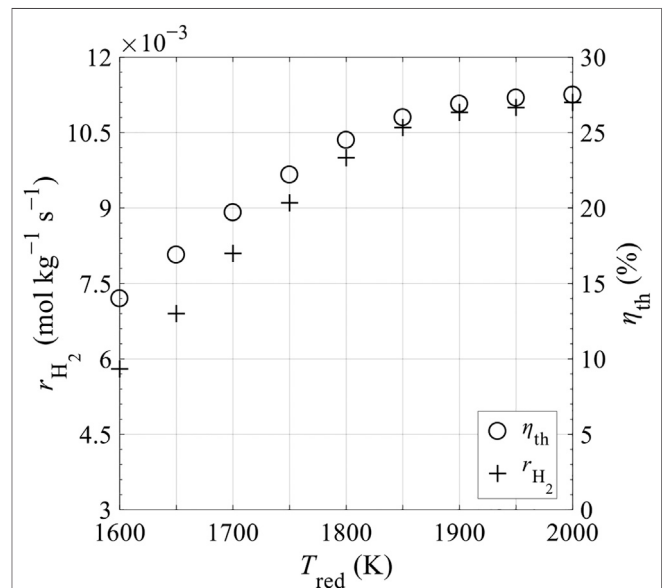


**FIGURE 13 |** Hydrogen production rate per kilogram of ceria,  $r_{\text{H}_2}$ , and total solar-to-fuel efficiency,  $\eta_{\text{th}}$ , as a function of reduction temperature  $T_{\text{red}}$ .

recuperation process,  $\delta_{\text{present}}$  exceed the values of  $\delta$  under the equilibrium condition,  $\delta_{\text{eq}}$  except for the initial and final states of cycles.

To examine the effect of the assumption of linear change of  $\delta$  in the recuperation process, we introduce a correction factor  $\alpha$  varying from 0 to 1. Instead of setting  $\delta$  to  $\delta_{\text{eq}}$  for the initial and final points of each cycle (marked with squares),  $\delta$  is reduced to  $\delta_{\text{revised}} = \alpha\delta_{\text{eq}}$  (marked with asterisks).  $\alpha$  is adjusted by the trial-and-error method for different cavity positions to

ensure  $\delta_{\text{revised}}$  is always below  $\delta_{\text{eq}}$ , namely  $\Delta G \leq 0$ . **Figure 9B** shows results of solar-to-fuel efficiencies using this correction for different numbers of pre-heating cavities. It is found that  $\eta_{\text{th, present}}$  is larger than  $\eta_{\text{th, revised}}$  due to the overestimation caused by neglecting the limit of the second law. However, the difference between the two efficiencies,  $\Delta\eta_{\text{th}}$ , is less than 0.3%. The relative error  $\sigma_{\text{eff}}$  is  $\sim 1\%$  for  $N \leq 6$ , and further decreases to  $\sim 0.5\%$  for  $N > 6$ . The

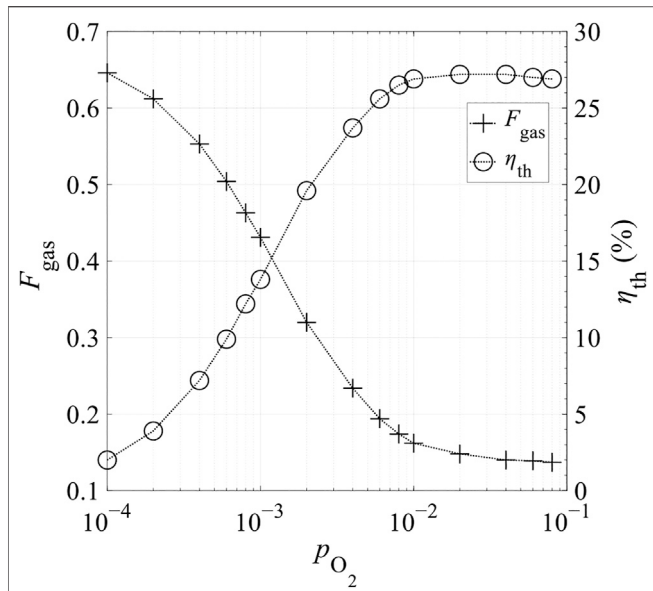


**FIGURE 14** | Heat loss fraction corresponding to gas-phase heat recovery,  $F_{\text{gas}}$ , and total thermal efficiency  $\eta_{\text{th}}$  as a function of relative oxygen partial pressure at the end of reduction,  $p_{\text{O}_2}$ .

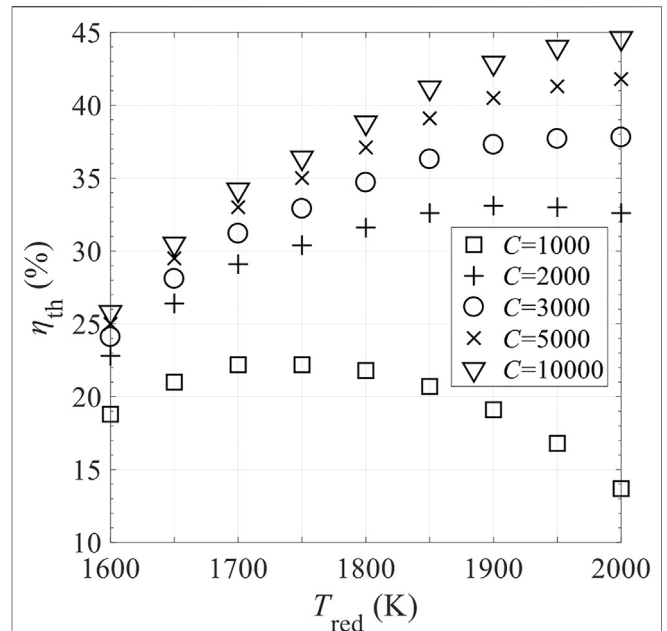


**FIGURE 16** | Effect of concentration ratio  $C$  on total solar-to-fuel efficiency  $\eta_{\text{th}}$  in different levels of reduction temperature,  $T_{\text{red}}$ , with perfect gas-phase heat recovery and relative oxygen partial pressure  $p_{\text{O}_2}$  of  $5 \times 10^{-6}$ .

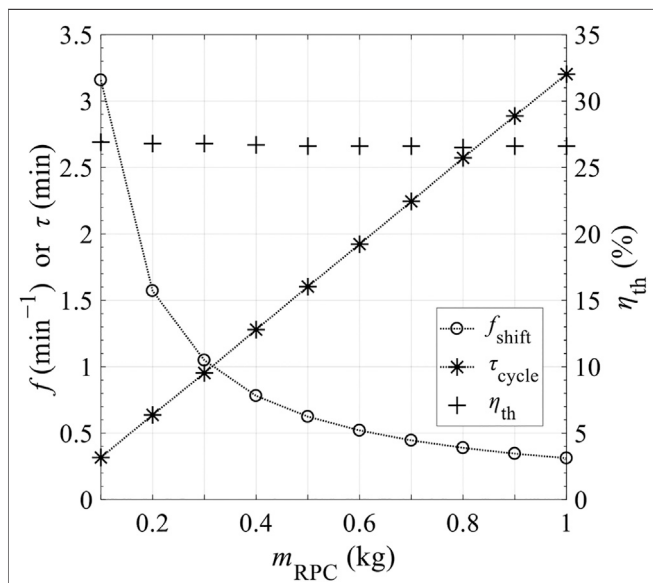


**FIGURE 15** | Shifting frequency of secondary mirror,  $f$ , or reaction duration,  $\tau$ , and total solar-to-fuel efficiency,  $\eta_{\text{th}}$ , as a function of mass of ceria in CRR,  $m_{\text{RPC}}$ .

linear assumption greatly increases the computational efficiency of the model with satisfactory accuracy. Hence, it is used to make the following predictions of the system performance.

### Recuperation Unit

We first present the results of thermodynamic parameters, including temperature, relative oxygen partial pressure, and

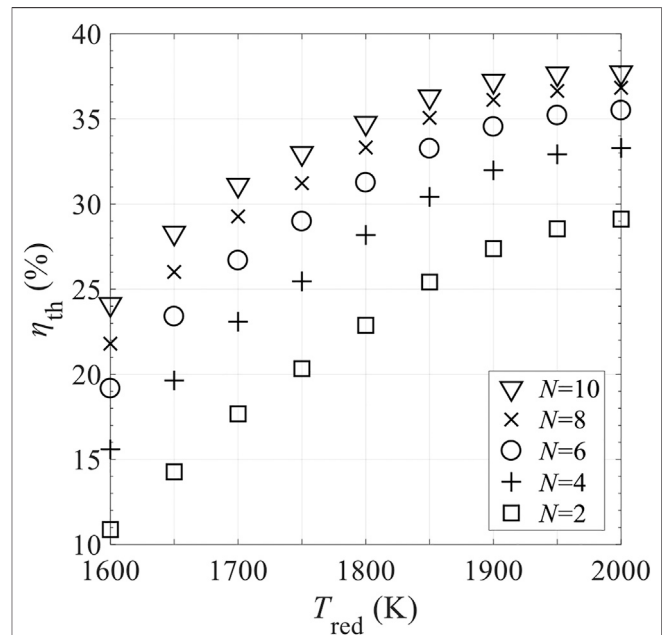


**FIGURE 17** | Effect of number of CRRs in the pre-cooling and pre-heating zones,  $N$ , on total solar-to-fuel efficiency  $\eta_{\text{th}}$  in different levels of reduction temperature,  $T_{\text{red}}$ , with perfect gas-phase heat recovery and relative oxygen partial pressure  $p_{\text{O}_2}$  of  $5 \times 10^{-6}$ .

the non-stoichiometric number of ceria in CRRs in the recuperation unit when a steady state is reached.

The temperature distribution of CRRs in the recuperation unit is depicted in **Figure 10**. The recuperation unit consists of a cascade of

20 CRR positions, and the indexing numbers  $i$  of the CRRs in the pre-cooling and pre-heating parts correspond to #1–10 and #11–20, respectively. For  $1 \leq i \leq 10$ , the temperature of the CRR in # $i$  position drops from  $T_i^{(n-1)}$  (State 1) to  $T_i^{(n)}$  (State 4) after a complete cycle. The sensible heat in CRRs of the pre-cooling zone is captured and transported to the CRRs in the pre-heating part via the  $N_2$  sweep flow. Therefore, for  $11 \leq i \leq 20$ , the CRR temperature increase is synchronized. **Figure 10** also shows that the temperature peaks in the middle for  $i = 10$  and decreases toward both sides. After 20 cycles, the target CRR, initially located in position #20, passes through all CRR positions and eventually arrives at position #1. The process can be separated into two stages. For the first 10 cycles, the temperature of the target CRR climbs up gradually. A peak value of 1,730 K can be reached at position #11 of the pre-heating part. For the next 10 cycles, the target CRR is cooled down step by step from the reduction temperature,  $T_{\text{red}} = 1900$  K. The minimum value, 1038 K, is obtained as the CRR moves to position #1. The small temperature difference between  $T_1$  and  $T_{\text{ox}}$  reduces the quenched heat loss,  $Q_{\text{quench}}$ , prior to the water-splitting process. Therefore, a high solid-phase heat recovery efficiency of 81% can be reached, as calculated by **Eq. 25**.

**Figure 11** shows the thermodynamic parameters  $\delta$  and  $p_{O_2}$  as a function of recuperation CRR position at the end of a cycle. Pre-reduction may occur in the CRRs of the pre-heating part ( $11 \leq i \leq 20$ ).  $\delta$  can increase rapidly and reach a peak value of 0.015 when  $i$  approaches 11. Because of pre-reduction,  $O_2$  is generated and gradually accumulated in the sweep gas.  $p_{O_2}$  of the gas flow increases from  $2.4 \times 10^{-3}$  to  $3.4 \times 10^{-3}$  when  $i$  varies from 11 to 20. The pre-reducing effect enables storing 10% of the sensible heat in the form of chemical energy by increasing  $\bar{h}_{O_2}$  ( $\delta$ ) during pre-heating. **Figure 11** shows that  $\delta$  can increase by 6% as compared to  $\delta_{\text{red}}$ , and finally reach 0.036.

## Sensitivity Analysis

Here we present the results of sensitivity study relative to change of a single key parameter, including number of CRRs in the pre-cooling or pre-heating part,  $N$ , reduction temperature  $T_{\text{red}}$ , relative oxygen partial pressure at the end of reduction  $p_{O_2}$ , and mass of RPC per cavity  $m_{\text{RPC}}$ , on the receiver–reactor array performance characterized by solid-phase heat recovery effectiveness  $\varepsilon_{\text{solid}}$ , solar-to-fuel efficiency  $\eta_{\text{th}}$ , hydrogen production rate  $r_{H_2}$ , gas-phase heat recovery loss fraction  $F_{\text{gas}}$ , and reaction duration  $\tau$ . Then, the results of sensitivity study of the effects of changing parameters, including concentration ratio,  $C$ , gas-phase heat recovery effectiveness,  $\varepsilon$ ,  $N$ ,  $T_{\text{red}}$ , and  $p_{O_2}$ , respectively, on the system performance are presented.  $C$  directly affects the cavity radiative heat loss,  $Q_{\text{rad}}$ . Increasing  $C$  decreases  $Q_{\text{rad}}$  for the same  $T_{\text{red}}$ .  $N$  and  $\varepsilon$  are key factors influencing the heat recovery efficiency during gas-solid- and gas-gas-phase heat exchange.  $T_{\text{red}}$  and  $p_{O_2}$  are the driving forces for reduction and affect the cavity heat loss and the heat recovery efficiency during gas-phase heat exchange.

According to **Figure 12**,  $\varepsilon_{\text{solid}}$  and  $\eta_{\text{th}}$  vary from 63% and 15% to 83% and 30%, respectively, by increasing  $N$  from 2 to 16. This is because that a large  $N$  leads to a small temperature difference between the reduction CRR and the CRR in #(N+1) position, namely ( $T_{\text{red}} - T_{N+1}$ ), which improves the solid-phase heat recovery and thus the total solar-to-fuel efficiency. The improvement magnitude is relatively larger when  $N$  is increased from 2 to 4 that  $\varepsilon_{\text{solid}}$  and  $\eta_{\text{th}}$  are increased

by 17% and 33%, respectively.  $\varepsilon_{\text{solid}}$  and  $\eta_{\text{th}}$  increase with  $N$  at diminishing rates, as limited by other factors such as  $T_{\text{red}}$ ,  $p_{O_2}$ ,  $\varepsilon$ , and  $C$ . On the other hand, a large  $N$  also leads to a large required CRR disk diameter, and thereby a large tilt angle of the tower reflector axis, decreasing the system optical efficiency (Li et al., 2020b). Here,  $N$  is set to 10 in the baseline receiver–reactor system.

**Figure 13** shows the increase of hydrogen production rate per kilogram of ceria,  $r_{H_2}$ , and total solar-to-fuel efficiency,  $\eta_{\text{th}}$ , with reduction temperature,  $T_{\text{red}}$ , which is attributed to the robust reduction capacity of non-stoichiometric ceria at high temperatures. The rate and efficiency increases are slower when  $T_{\text{red}}$  further increases due to the rapidly increasing emission losses. For example, increasing  $T_{\text{red}}$  from 1,600 to 1,700 K yields the increment of  $r_{H_2}$  and  $\eta_{\text{th}}$ ,  $2.3 \times 10^{-3} \text{ mol kg}^{-1} \text{ s}^{-1}$  and 5.7%, respectively, whereas increasing  $T_{\text{red}}$  from 1,900 to 2,000 K yields the increment of  $r_{H_2}$  and  $\eta_{\text{th}}$  of only  $0.2 \times 10^{-3} \text{ mol kg}^{-1} \text{ s}^{-1}$  and 0.6%, respectively. The improvement in the total thermal performance is insignificant for  $T_{\text{red}} > 1,900$  K.

The relative oxygen partial pressure,  $p_{O_2}$ , also affects the thermal performance of the receiver–reactor system. As previously mentioned, ceria reduction is favored at atmosphere of low  $p_{O_2}$ , which can be created by a certain flow of pure  $N_2$  to keep removing  $O_2$  generated in the ceria. The benefit gained by reducing  $p_{O_2}$  should be weighed against the penalty of thermal losses associated with imperfect gas-phase heat recovery. **Figure 14** shows solar-to-fuel efficiency,  $\eta_{\text{th}}$ , and gas-phase heat recovery loss fraction,  $F_{\text{gas}}$ , as a function of  $p_{O_2}$ . A peak  $\eta_{\text{th}}$  of 27% is found at relatively high  $p_{O_2}$  (0.01–0.1). As  $p_{O_2}$  decreases, the gas-phase heat recovery loss gradually becomes the major factor of system heat losses, and  $\eta_{\text{th}}$  declines sharply.  $F_{\text{gas}}$  rapidly increases from 0.14 to 0.65 when  $p_{O_2}$  drops from 0.08 to  $10^{-4}$ .  $\eta_{\text{th}}$  is only 2% at  $p_{O_2} = 10^{-4}$ .

**Figure 15** shows the effects of the mass of RPC,  $m_{\text{RPC}}$ , on reaction duration per cycle,  $\tau$ , shifting frequency of reactor disk  $f = 1/\tau$ , and thermal efficiency  $\eta_{\text{th}}$ .  $\tau$  is proportional to  $m_{\text{RPC}}$ , indicating that for higher  $m_{\text{RPC}}$ , longer time is needed to finalize the reaction, and the required  $f$  is lower. Based on **Figure 15**,  $m_{\text{RPC}}$  has little impact on  $\eta_{\text{th}}$ . **Figures 16, 17** show the effects of  $C$  and  $N$  on  $\eta_{\text{th}}$  for selected values of  $T_{\text{red}}$  and assuming  $\varepsilon = 1$ .  $\eta_{\text{th}}$  is calculated based on selected  $T_{\text{red}}$  varying from 1600 to 2000 K in 50 K increments for a fixed  $p_{O_2}$  of  $5 \times 10^{-5}$ . As shown in **Figure 16**, optimal  $T_{\text{red}}$  for maximized  $\eta_{\text{th}}$  increases with the increase of  $C$ . Peak values of  $\eta_{\text{th}}$  are found at  $T_{\text{red}}$  of between 1,600 and 2,000 K for  $C \leq 3,000$ . For instance, for  $C = 1,000, 2,000$ , and 3,000, the maximum  $\eta_{\text{th}}$  of 22%, 33%, and 38%, respectively, are obtained at  $T_{\text{red}} = 1700$  K, 1900 K, and 2,000 K. Further increasing  $C$  leads to higher optimal  $T_{\text{red}}$  and the corresponding  $\eta_{\text{th}}$ .  $\eta_{\text{th}}$  increases at a diminishing rate with  $C$ . Moreover, aiming at high  $C$  can lower optical efficiency of the optical sub-system (Li et al., 2016; Li et al., 2020a; Li et al., 2020b). **Figure 17** shows that  $\eta_{\text{th}}$  increases monotonically with increasing  $T_{\text{red}}$  for given  $N$ . The maximum  $\eta_{\text{th}}$  of 29%, 33%, 35%, 37%, and 38% are obtained at maximum  $T_{\text{red}} = 2,000$  K, corresponding to  $N = 2, 4, 6, 8$  and 10, respectively. Increasing  $N$  leads to higher  $\eta_{\text{th}}$  under the fixed  $T_{\text{red}}$  and  $p_{O_2}$ , but  $\eta_{\text{th}}$  increases at a diminishing rate with  $N$ . For instance,  $\eta_{\text{th}}$  grows 4.6% and 1.1%, when increasing  $N$  from 2 to 4, and 8 to 10 at  $T_{\text{red}} = 1,900$  K, respectively. In addition, as mentioned in Section 5.2, increasing  $N$  leads to a larger tilt angle of the tower reflector axis and reduces the optical efficiency of the system (Li et al., 2020b).



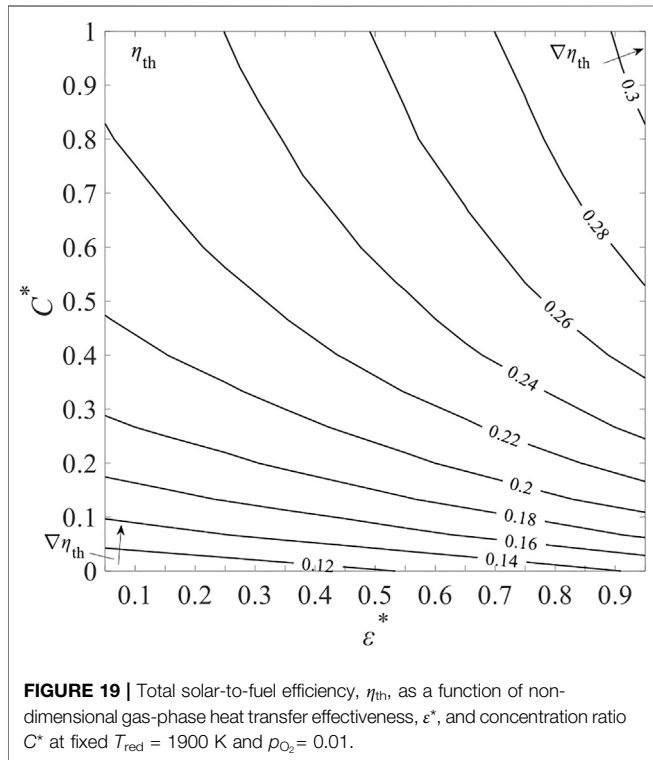
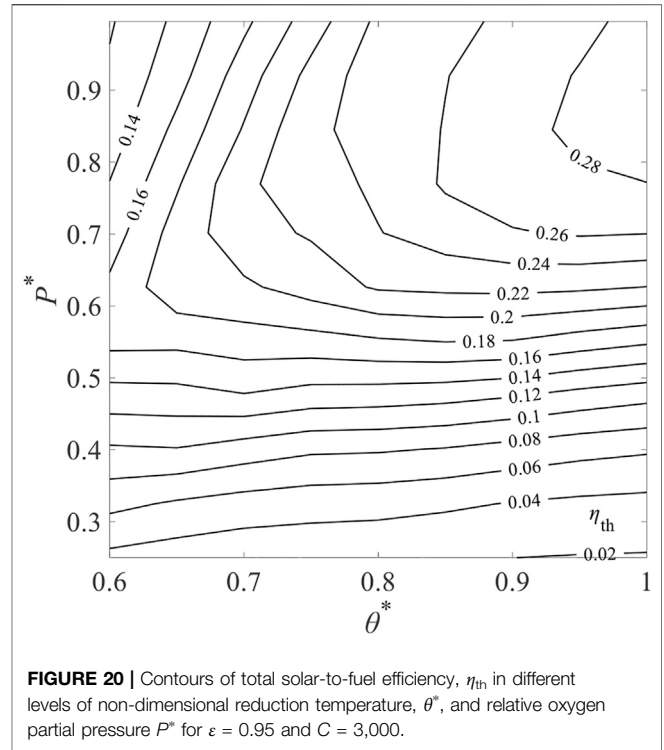
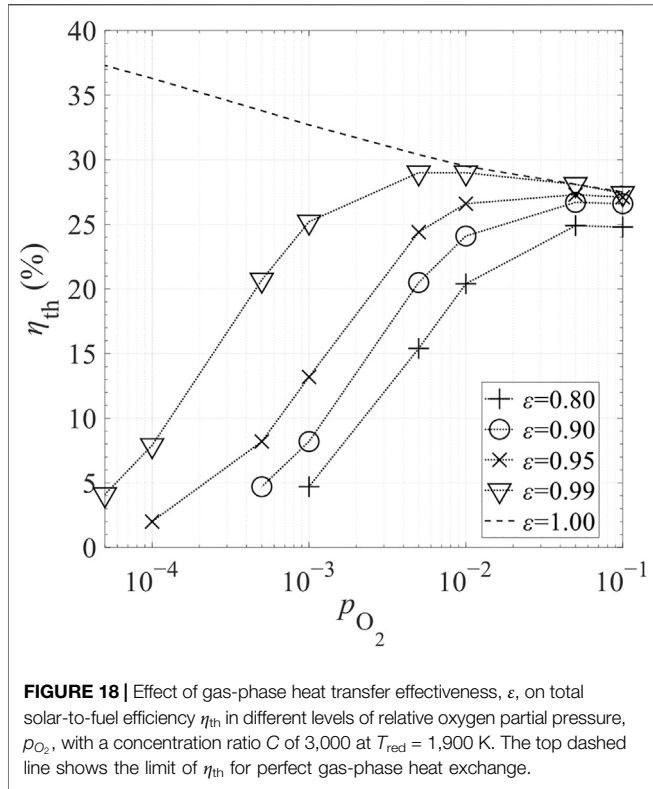


**Figure 18** shows the effects of  $\epsilon$  on total solar-to-fuel efficiency,  $\eta_{th}$ , for selected  $p_{O_2}$  varying from  $5 \times 10^{-5}$  to 0.1. The dashed line shows the limit of  $\eta_{th}$  for perfect gas-phase heat exchange, namely  $\epsilon = 1$ . Without the gas-phase heat recovery loss,  $\eta_{th}$  increases

logarithmically with  $p_{O_2}$ , namely  $\eta_{th} = f(\ln p_{O_2})$ . A peak value of  $\eta_{th}$  of 37% is obtained at the lowest simulated  $p_{O_2}$  of  $5 \times 10^{-5}$ . For  $\epsilon < 1$ , the gas-phase heat recovery loss reduces  $\eta_{th}$ . It is found that the overall thermal performance of the receiver-reactor system is sensitive to  $\epsilon$ , and  $\epsilon$  may become a dominant factor of  $\eta_{th}$ , especially at low  $p_{O_2}$  levels. For instance,  $\eta_{th}$  approaches the limit of 33% for  $\epsilon = 1$ , but is only 5% for  $\epsilon = 0.8$  when  $p_{O_2} = 10^{-3}$ . Except for  $\epsilon = 1$ ,  $\eta_{th}$  rapidly decreases for all cases of  $p_{O_2} < 10^{-3}$ . As an example of  $\epsilon = 0.95$ ,  $\eta_{th}$  drops from 24% down to 2% when decreasing  $p_{O_2}$  from  $5 \times 10^{-3}$  to  $10^{-4}$ . This is because the gas-phase heat recovery loss is positively correlated to  $\dot{m}_{N_2}$  and thus varies inversely to  $p_{O_2}$  (as shown in **Eq. 16**). Therefore, reducing  $p_{O_2}$  at a low level may not lead to improved efficiency because the increased gas-phase heat recovery loss outweighs the thermodynamic benefits gained from the increase in reduction extent. The optimal values of  $p_{O_2}$  are found at a relatively large  $p_{O_2}$  level of  $\sim 0.01$ , in which the heat recovery loss becomes a minor impact factor. Correspondingly,  $\eta_{th}$  approaches its maximum with the optimal  $p_{O_2}$ . For instance, a peak value over 27% is obtained at  $p_{O_2} = 0.05$  for  $\epsilon = 0.95$ .

**Figure 19** shows the contour map of  $\eta_{th}$  for selected  $\epsilon$  varying from 0.81 to 0.99 and  $C$  from 1,000 to 4,000 at  $T_{red} = 1900$  K and  $p_{O_2} = 0.01$ . For the sake of comparison, normalized variables  $\epsilon^*$  and  $C^*$  are defined as

$$\epsilon^* = \frac{\epsilon - \epsilon_{min}}{\epsilon_{max} - \epsilon_{min}}; C^* = \frac{C - C_{min}}{C_{max} - C_{min}} \quad (27)$$

where  $\epsilon_{min}$ ,  $\epsilon_{max}$  and  $C_{min}$ ,  $C_{max}$  are set to 0.8, 1 and 1,000, 4,000, respectively. The colored contour lines present the different levels of  $\eta_{th}$ . The gradient of  $\eta_{th}$  is given by  $\nabla \eta_{th} = \left( \frac{\partial \eta_{th}}{\partial \epsilon^*} \right) \vec{i} + \left( \frac{\partial \eta_{th}}{\partial C^*} \right) \vec{j}$ .

As shown in **Figure 19**,  $\eta_{th}$  increases when increasing  $C^*$  or  $\varepsilon^*$ . The maximum and minimum values of  $\eta_{th}$  are 31% and 10%, which are found at (0.95, 1) and (0.05, 0), respectively. The magnitude of the gradient of  $\eta_{th}$ ,  $|\nabla\eta_{th}|$ , decreases when increasing  $C^*$  or decreasing  $\varepsilon^*$ .  $|\nabla\eta_{th}|_{max}$  and  $|\nabla\eta_{th}|_{min}$  are 0.68 and 0.07, obtained at (0.95, 0) and (0.05, 1). For the region of low  $C^*$ ,  $\left(\frac{\partial\eta_{th}}{\partial C^*}\right)$  is much larger than  $\left(\frac{\partial\eta_{th}}{\partial\varepsilon^*}\right)$ .  $\nabla\eta_{th}$  tends to point upwards. For instance,  $\left(\frac{\partial\eta_{th}}{\partial C^*}\right)$  equals 0.5 at  $\varepsilon^* = 0.05$ ,  $C^* = 0$ , which is fourteen times higher than  $\left(\frac{\partial\eta_{th}}{\partial\varepsilon^*}\right)$ . Hence,  $C^*$  is the critical parameter for  $\eta_{th}$  for low  $C^*$ .

As  $C^*$  increases,  $\left(\frac{\partial\eta_{th}}{\partial\varepsilon^*}\right)/\left(\frac{\partial\eta_{th}}{\partial C^*}\right)$  will gradually increase. It approaches 2.4 and 2.3 at  $\varepsilon^* = 0.05$  and 0.95, when  $C^* = 1$ . Since  $\eta_{th}$  is more sensitive to the change of  $\varepsilon^*$  rather than  $C^*$  for high  $C^*$ ,  $\varepsilon^*$  is more important than  $C^*$  for  $\eta_{th}$  under these conditions.

**Figure 20** shows the contour map of  $\eta_{th}$  for selected  $T_{red}$  varying from 1,600 to 2,000 K and  $p_{O_2}$  from  $10^{-4}$  to 0.096 when  $\varepsilon = 0.95$  and  $C = 3,000$ . Non-dimensional reduction temperature and relative oxygen partial pressure,  $\theta^*$  and  $P^*$ , are defined as

$$\theta^* = \frac{T_{red} - T_{min}}{T_{max} - T_{min}}; P^* = \frac{\ln(p_{O_2}/p_{O_2,min})}{\ln(p_{O_2,max}/p_{O_2,min})} \quad (28)$$

where  $p_{O_2,min}$ ,  $p_{O_2,max}$  and  $T_{min}$ ,  $T_{max}$  are set to  $10^{-5}$ , 0.1 and 1,000, 2,000 K, respectively. As shown in **Figure 20**,  $\eta_{th}$  is low for low  $P^*$ . The values are less than 4% for  $P^* = 0.25$ . For the range  $0.25 \leq P^* \leq 0.55$ , increasing  $p_{O_2}$  improves  $\eta_{th}$ . For instance, when increasing  $P^*$  from 0.25 to 0.55 for  $\theta^* = 1$ ,  $\eta_{th}$  is gradually improved from 2% to 16%. The average growth rate of  $\eta_{th}$  is 0.29 for the increase from 2% to 6%, which is then improved to 0.67 for the increase from 6% to 16%. By contrast,  $\eta_{th}$  is much less sensitive to the change of  $\theta^*$  for low  $P^*$ . The differences of  $\eta_{th}$  are <2% when varying  $\theta^*$  over the range of 0.6–1 for  $P^* = 0.25$ . As  $P^*$  increases over 0.55, the increasing magnitude of  $\eta_{th}$  along the  $y$ -axis slows down. Meanwhile, the influence of  $\theta^*$  on  $\eta_{th}$  is enhanced.  $\theta^*$  becomes the major factor for  $\eta_{th}$  when further increasing  $P^*$  to high values. For the range of high  $P^*$  and low  $\theta^*$ , increasing  $\theta^*$  may lead to a rapid increase of  $\eta_{th}$ . It is shown that  $\eta_{th}$  is doubled as  $\theta^*$  increases from 0.6 to 0.8 for  $P^* = 1$ , while the change in  $\eta_{th}$  is insignificant for  $P^*$  between 0.92 and 1 and  $\theta^* = 0.6$ . In addition, the gradient of  $\eta_{th}$  points downwards in the region of high  $P^*$  and  $\theta^*$  toward a point corresponding to the optimal solution with the maximum of  $\eta_{th} = 29\%$  at  $\theta^* = 1$  and  $P^* = 0.85$ .

## CONCLUSION

In this study, a conceptual fixed-bed solar thermochemical cavity receiver–reactor array has been proposed and numerically studied for water-splitting via ceria-based redox cycling. Heat recuperation was modeled by a linear matrix model while reduction and oxidation were modeled by a lumped parameter model. Thermal performance characterized by solid-phase heat

recovery effectiveness and total solar-to-fuel efficiency was studied for selected parameters of the proposed system such as the reduction temperature, relative oxygen partial pressure, number of receiver–reactor, concentration ratio, and gas-phase heat recovery effectiveness.

Under the assumptions made in this study, the solid-phase heat recovery effectiveness and the total solar-to-fuel efficiency were found to be 80% and 27%, respectively, for the baseline system. Along with the pre-heating process, pre-reduction occurs simultaneously, resulting in ceria non-stoichiometry of 0.015, which was attributed to the dual function of  $N_2$  as HTF and oxygen scavenger during recuperation. A solar-to-fuel efficiency of 27% was found with a reduction temperature at 1,900 K and relative oxygen partial pressure of 0.01. The concentration ratio and gas-phase heat recovery effectiveness for the baseline case were assumed to be 3,000 and 0.95, respectively. A higher thermal efficiency can be achieved by increasing the total number of receiver–reactors.

Sensitivity analysis demonstrated that the solar-to-fuel efficiency is highly sensitive to the concentration ratio and the gas-phase heat recovery effectiveness at high reduction temperature and low relative oxygen partial pressure conditions. Increasing the concentration ratio and gas-phase heat recovery effectiveness simultaneously improves the system performance. The total solar-to-fuel efficiency was found to be 42% with a concentration ratio of 5,000 and perfect gas-phase heat recovery. In addition, for the baseline values of the concentration ratio and the gas-phase heat recovery effectiveness, the overall solar-to-fuel efficiency can be effectively increased by increasing relative oxygen partial pressure at low temperature or by increasing temperature at high relative oxygen partial pressure.

## DATA AVAILABILITY STATEMENT

The raw data supporting the conclusions of this article will be made available by the authors, without undue reservation.

## AUTHOR CONTRIBUTIONS

SY concept, analysis, writing. LL concept, writing. BW writing. SL writing. JW funding, supervision, writing. PL writing. WL funding, supervision, concept, writing.

## FUNDING

This work was supported by the National Natural Science Foundation of China (No. 51736006), the Scientific Research Foundation of Graduate School of Southeast University (No. YBPY 1855), the China Scholarship Council (SY, Grant No. (2017)3109), the Australian Renewable Energy Agency (Grant No. 2014/RND005), and the Australian Research Council (Grant No. FT140101213).

## REFERENCES

- Abanades, S., Legal, A., Cordier, A., Peraudeau, G., Flamant, G., and Julbe, A. (2010). Investigation of Reactive Cerium-Based Oxides for H<sub>2</sub> Production by Thermochemical Two-step Water-Splitting. *J. Mater. Sci.* 45 (15), 4163–4173. doi:10.1007/s10853-010-4506-4
- Bader, R., and Lipiński, W. (2017). “Solar thermal processing,” in *Advances in Concentrating Solar Thermal Research and Technology*, Woodhead Publishing Series in Energy. Editors M. J. Blanco and L. R. Santigosa, (Berlin: Springer) 403–459.
- Bader, R., Venstrom, L. J., Davidson, J. H., and Lipiński, W. (2013). Thermodynamic Analysis of Isothermal Redox Cycling of Ceria for Solar Fuel Production. *Energy Fuels* 27 (9), 5533–5544. doi:10.1021/ef400132d
- Blank, D. A., and Wu, C. (1994). Power Potential of a Terrestrial Solar-Radiant Stirling Heat Engine. *Int. J. Ambient Energ.* 15 (3), 131–139. doi:10.1080/01430750.1994.9675645
- Chueh, W. C., and Haile, S. M. (2010). A Thermochemical Study of Ceria: Exploiting an Old Material for New Modes of Energy Conversion and CO<sub>2</sub> mitigation. *Mathematical, Physical and Engineering Sciences* 368. *Philos. Trans. A. Math. Phys. Eng. Sci.* 368, 3269–3294. doi:10.1098/rsta.2010.0114
- Chueh, W. C., Falter, C., Abbott, M., Scipio, D., Furler, P., Haile, S. M., et al. (2010). High-Flux Solar-Driven Thermochemical Dissociation of CO<sub>2</sub> and H<sub>2</sub>O Using Nonstoichiometric Ceria. *Science* 330 (6012), 1797–1801. doi:10.1126/science.1197834
- Dähler, F., Wild, M., Schäppi, R., Haueter, P., Cooper, T., Good, P., et al. (2018). Optical Design and Experimental Characterization of a Solar Concentrating Dish System for Fuel Production via Thermochemical Redox Cycles. *Solar Energy* 170, 568–575. doi:10.1016/j.solener.2018.05.085
- Diver, R. B., Miler, J. E., Siegel, N. P., and Moss, T. A. (2010). “Testing of a CR5 Solar Thermochemical Heat Engine Prototype,” in Proceedings of the ASME 2010 4th International Conference on Energy Sustainability Volume 2, 97–104.
- El-Ehwany, A. A., Hennes, G. M., Eid, E. I., and El-Kenany, E. A. (2010). Development of the Performance of an Alpha-type Heat Engine by Using Elbow-bend Transposed-Fluids Heat Exchanger as a Heater and a Cooler. *Eng. Convers. Manage.* 52 (2), 1010–1019. doi:10.1016/j.enconman.2010.08.029
- Ermanoski, I., Siegel, N. P., and Stechel, E. B. (2013). A New Reactor Concept for Efficient Solar-Thermochemical Fuel Production. *J. Sol. Energy Eng.* 135 (3), 031002. doi:10.1115/1.4023356
- Falter, C. P., Sizmann, A., and Pitz-Paal, R. (2015). Modular Reactor Model for the Solar Thermochemical Production of Syngas Incorporating Counter-flow Solid Heat Exchange. *Sol. Energy* 122, 1296–1308. doi:10.1016/j.solener.2015.10.042
- Furler, P., Scheffe, J., Gorbar, M., Moes, L., Vogt, U., and Steinfeld, A. (2012a). Solar Thermochemical CO<sub>2</sub> Splitting Utilizing a Reticulated Porous Ceria Redox System. *Energy Fuels* 26 (11), 7051–7059. doi:10.1021/ef3013757
- Furler, P., Scheffe, J. R., and Steinfeld, A. (2012b). Syngas Production by Simultaneous Splitting of H<sub>2</sub>O and CO<sub>2</sub> via Ceria Redox Reactions in a High-Temperature Solar Reactor. *Energy Environ. Sci.* 5 (3), 6098–6103. doi:10.1039/c1ee02620h
- Haeussler, A., Abanades, S., Julbe, A., Jouannaux, J., and Cartoixa, B. (2020). Solar Thermochemical Fuel Production from H<sub>2</sub>O and CO<sub>2</sub> Splitting via Two-step Redox Cycling of Reticulated Porous Ceria Structures Integrated in a Monolithic Cavity-type Reactor. *Energy* 201, 117649. doi:10.1016/j.energy.2020.117649
- Hao, Y., Yang, C.-K., and Haile, S. M. (2014). Ceria-Zirconia Solid Solutions (Ce<sub>1-x</sub>Zr<sub>x</sub>O<sub>2-δ</sub>, X ≤ 0.2) for Solar Thermochemical Water Splitting: A Thermodynamic Study. *Chem. Mater.* 26, 6073–6082. doi:10.1021/cm503131p
- Häring, H. W. (2008). *The Air Gases Nitrogen, Oxygen and Argon, Industrial Gases Processing*. Hoboken: John Wiley & Sons, 9–109.
- Hathaway, B. J., Bala Chandran, R., Gladen, A. C., Chase, T. R., and Davidson, J. H. (2016). Demonstration of a Solar Reactor for Carbon Dioxide Splitting via the Isothermal Ceria Redox Cycle and Practical Implications. *Energy Fuels* 30, 6654–6661. doi:10.1021/acs.energyfuels.6b01265
- Lapp, J., Davidson, J. H., and Lipiński, W. (2013). Heat Transfer Analysis of a Solid-Solid Heat Recuperation System for Solar-Driven Nonstoichiometric Redox Cycles. *J. Sol. Energy Eng.* 135 (3), 031004. doi:10.1115/es2012-91078
- Lapp, J., Davidson, J. H., and Lipiński, W. (2012). Efficiency of Two-step Solar Thermochemical Non-stoichiometric Redox Cycles with Heat Recovery. *Energy* 37, 591–600. doi:10.1016/j.energy.2011.10.045
- Lapp, J., and Lipiński, W. (2014). Transient Three-Dimensional Heat Transfer Model of a Solar Thermochemical Reactor for H<sub>2</sub>O and CO<sub>2</sub> Splitting via Nonstoichiometric Ceria Redox Cycling. *J. Sol. Energy Eng.* 136 (3), 031006. doi:10.1115/1.4026465
- Li, L., Coventry, J., Bader, R., Pye, J., and Lipiński, W. (2016). Optics of Solar Central Receiver Systems: a Review. *Opt. Express* 24 (14), A985–A1007. doi:10.1364/oe.24.00a985
- Li, L., Wang, B., Pye, J., and Lipiński, W. (2020a). Temperature-based Optical Design, Optimization and Economics of Solar Polar-Field Central Receiver Systems with an Optional Compound Parabolic Concentrator. *Sol. Energy* 206, 1018–1032. doi:10.1016/j.solener.2020.05.088
- Li, L., Yang, S., Wang, B., Pye, J., and Lipiński, W. (2020b). Optical Analysis of a Solar Thermochemical System with a Rotating tower Reflector and a Receiver-Reactant Array. *Opt. Express* 28, 19429–19445. doi:10.1364/oe.389924
- Li, S., Wheeler, V. M., Kreider, P. B., Bader, R., and Lipiński, W. (2018a). Thermodynamic Analyses of Fuel Production via Solar-Driven Nonstoichiometric Metal Oxide Redox Cycling. Part 2. Impact of Solid-Gas Flow Configurations and Active Material Composition on System-Level Efficiency. *Energy Fuels* 32 (10), 10848–10863. doi:10.1021/acs.energyfuels.8b02082
- Li, S., Wheeler, V. M., Kreider, P. B., and Lipiński, W. (2018b). Thermodynamic Analyses of Fuel Production via Solar-Driven Non-stoichiometric Metal Oxide Redox Cycling. Part 1. Revisiting Flow and Equilibrium Assumptions. *Energy Fuels* 32 (10), 10838–10847. doi:10.1021/acs.energyfuels.8b02081
- Li, S., Wheeler, V. M., Kumar, A., Venkataraman, M. B., Muhich, C. L., Hao, Y., et al. (2021). Thermodynamic Guiding Principles for Designing Nonstoichiometric Redox Materials for Solar Thermochemical Fuel Production: Ceria, Perovskites, and beyond. *Energy Technol.* 14, 2000925. doi:10.1002/ente.202000925
- Marxer, D., Furler, P., Takacs, M., and Steinfeld, A. (2017). Solar Thermochemical Splitting of CO<sub>2</sub> into Separate Streams of CO and O<sub>2</sub> with High Selectivity, Stability, Conversion, and Efficiency. *Energy Environ. Sci.* 10, 1142–1149. doi:10.1039/c6ee03776c
- Miller, J. E., McDaniel, A. H., and Allendorf, M. D. (2014). Considerations in the Design of Materials for Solar-Driven Fuel Production Using Metal-Oxide Thermochemical Cycles. *Adv. Energy Mater.* 4, 1300469. doi:10.1002/aenm.201300469
- Muhich, C. L., Blaser, S., Hoes, M. C., and Steinfeld, A. (2018). Comparing the Solar-To-Fuel Energy Conversion Efficiency of Ceria and Perovskite Based Thermochemical Redox Cycles for Splitting H<sub>2</sub>O and CO<sub>2</sub>. *Int. J. Hydrogen Energy* 43, 18814–18831. doi:10.1016/j.ijhydene.2018.08.137
- Muhich, C. L., Ehrhart, B. D., Al-Shankiti, I., Ward, B. J., Musgrave, C. B., and Weimer, A. W. (2016). A Review and Perspective of Efficient Hydrogen Generation via Solar thermal Water Splitting. *Wires Energy Environ.* 5 (3), 261–287. doi:10.1002/wene.174
- Panlener, R. J., Blumenthal, R. N., and Garnier, J. E. (1975). A Thermodynamic Study of Nonstoichiometric Cerium Dioxide. *J. Phys. Chem. Sol.* 36 (11), 1213–1222. doi:10.1016/0022-3697(75)90192-4
- Qian, X., He, J., Mastronardo, E., Baldassarri, B., Yuan, W., Wolvertson, C., et al. (2021). Outstanding Properties and Performance of CaTi<sub>0.5</sub>Mn<sub>0.5</sub>O<sub>3-δ</sub> for Solar-Driven Thermochemical Hydrogen Production. *Matter* 4 (2), 688–708. doi:10.1016/j.matt.2020.11.016
- Siegel, N. P., Miller, J. E., Ermanoski, I., Diver, R. B., and Stechel, E. B. (2013). Factors Affecting the Efficiency of Solar Driven Metal Oxide Thermochemical Cycles. *Ind. Eng. Chem. Res.* 52 (9), 3276–3286. doi:10.1021/ie400193q
- Steinfeld, A. (2019). Concentrated Solar Energy - the Path for Efficient thermal Conversion to Power and Fuels. *Sci. Bull.* 64 (8), 485–486. doi:10.1016/j.scib.2019.04.012
- Steinfeld, A., Furler, P., Haselbacher, A., and Geissbühler, L. (2019). A Thermochemical Reactor System for a Temperature Swing Cyclic Process with Integrated Heat Recovery and a Method for Operating the Same. Google Patents.
- Steinfeld, A. (2005). Solar Thermochemical Production of Hydrogen-A Review. *Solar Energy* 78 (5), 603–615. doi:10.1016/j.solener.2003.12.012

- Sun-to-liquid (2020). Available at: <https://www.sun-to-liquid.eu/> (Accessed September 10, 2020).
- Venstrom, L. J., De Smith, R. M., Bala Chandran, R., Boman, D. B., Krenzke, P. T., and Davidson, J. H. (2015). Applicability of an Equilibrium Model to Predict the Conversion of CO<sub>2</sub> to CO via the Reduction and Oxidation of a Fixed Bed of Cerium Dioxide. *Energy Fuels* 29, 8168–8177. doi:10.1021/acs.energyfuels.5b01865
- Wang, B., Li, L., Pottas, J. J., Bader, R., Kreider, P. B., Wheeler, V. M., et al. (2020). Thermal Model of a Solar Thermochemical Reactor for Metal Oxide Reduction. *J. Sol. Energy Eng.* 142 (5), 051002. <https://doi.org/10.1115/1.4046229>
- Wang, B., Li, L., Schäfer, F., Pottas, J. J., Kumar, A., Wheeler, V. M., et al. (2021). Thermal Reduction of Iron-Manganese Oxide Particles in a High-Temperature Packed-Bed Solar Thermochemical Reactor. *Chem. Eng. J.* 412 (C), 128255. doi:10.1016/j.cej.2020.128255
- Welte, M., Barhoumi, R., Zbinden, A., Scheffe, J. R., and Steinfeld, A. (2016). Experimental Demonstration of the Thermochemical Reduction of Ceria in a Solar Aerosol Reactor. *Ind. Eng. Chem. Res.* 55, 10618–10625. doi:10.1021/acs.iecr.6b02853
- Yuan, C., Jarrett, C., Chueh, W., Kawajiri, Y., and Henry, A. (2015). A New Solar Fuels Reactor Concept Based on a Liquid Metal Heat Transfer Fluid: Reactor Design and Efficiency Estimation. *Sol. Energy* 122, 547–561. doi:10.1016/j.solener.2015.08.019

**Conflict of Interest:** The authors declare that the research was conducted in the absence of any commercial or financial relationships that could be construed as a potential conflict of interest.

Copyright © 2021 Yang, Li, Wang, Li, Wang, Lund and Lipiński. This is an open-access article distributed under the terms of the Creative Commons Attribution License (CC BY). The use, distribution or reproduction in other forums is permitted, provided the original author(s) and the copyright owner(s) are credited and that the original publication in this journal is cited, in accordance with accepted academic practice. No use, distribution or reproduction is permitted which does not comply with these terms.

## NOMENCLATURE

$C$  concentration ratio  
 $c_p$  specific heat at constant pressure,  $\text{kJ kg}^{-1} \text{K}^{-1}$   
 $c_v$  specific heat at constant volume,  $\text{kJ kg}^{-1} \text{K}^{-1}$   
 $F$  heat loss fraction  
 $f$  shifting frequency,  $\text{min}^{-1}$   
 $\bar{h}$  molar specific enthalpy,  $\text{kJ mol}^{-1}$   
 $\Delta \bar{h}_{\text{O}_2}$  change in molar enthalpy of the non-stoichiometric ceria per  $n_{\text{O}_2}$ ,  $\text{kJ mol}^{-1}$   
 $\Delta T$  temperature difference  $T_{\text{red}} - T_{\text{ox}}$ , K  
 $M$  molar mass,  $\text{kg mol}^{-1}$   
 $m$  mass, kg  
 $\dot{m}$  mass flow rate,  $\text{kg s}^{-1}$   
 $n$  amount of substance, mol  
 $N$  cavity number in the pre-cooling (or pre-heating) part of recuperation zone  
 $p$  pressure, Pa  
 $p_{\text{O}_2}$  relative oxygen partial pressure  
 $P^*$  non-dimensional oxygen partial pressure defined in Eq. 28  
 $Q$  heat, kJ  
 $\dot{Q}$  power, kW  
 $r_{\text{O}_2}$  rates of oxygen production,  $\text{mL min}^{-1} \text{g}_{\text{ceria}}^{-1}$   
 $T$  temperature, K  
 $r$  gas flow rate per unit mass of ceria,  $\text{kg s}^{-1} \text{kg}_{\text{ceria}}^{-1}$

## GREEK SYMBOLS

$\alpha$  correction factor  
 $\varepsilon$  heat recovery effectiveness  
 $\beta$  non-dimensional number defined in Eq. 20  
 $\gamma$  non-dimensional number defined in Eq. 20  
 $\delta$  non-stoichiometry

$\varepsilon^*$  non-dimensional heat recovery effectiveness defined in Eq. 27  
 $\eta_{\text{th}}$  solar-to-fuel efficiency  
 $\theta^*$  non-dimensional reduction temperature defined in Eq. 28  
 $\xi$  non-dimensional number defined in Eq. 22  
 $\tau$  reaction duration per cycle, min  
 $\Delta \tau$  time step, s  
 $\chi$  relaxation factor  
 $\Delta \delta$  change in non-stoichiometry

## SUBSCRIPTS

**H** high  
**HX** heat exchange  
**L** low  
**chem** chemical item  
**gas** gas-phase transport heat loss  
**fuel** fuel  
**input** input  
**other** other heat loss  
**ox** oxidation  
**quench** quenching heat loss  
**rad** radiative heat loss  
**recovery** recovery of conductive heat loss  
**red** reduction  
**ref** reference  
**reject** rejecting heat loss  
**shift** shifted from the previous phase  
**solar** solar energy  
**solid** solid-phase  
**trans** transport item  
 $\infty$  ambient